

# Multi-Scale Single-Bit *RP-EMS* Synthesis for Advanced Propagation Manipulation through System-by-Design

G. Oliveri,<sup>(1)</sup> *Senior Member, IEEE*, P. Rocca,<sup>(1)(2)</sup> *Senior Member, IEEE*, M. Salucci,<sup>(1)</sup> *Senior Member, IEEE*, D. Erricolo,<sup>(4)</sup> *Fellow, IEEE*, and A. Massa,<sup>(3)(1)(5)</sup> *Fellow, IEEE*

<sup>(1)</sup> *ELEDIA Research Center (ELEDIA@UniTN - University of Trento)*

DICAM - Department of Civil, Environmental, and Mechanical Engineering

Via Mesiano 77, 38123 Trento - Italy

E-mail: {giacomo.oliveri, paolo.rocca, marco.salucci, andrea.massa}@unitn.it

Website: [www.eledia.org/eledia-unitn](http://www.eledia.org/eledia-unitn)

<sup>(2)</sup> *ELEDIA Research Center (ELEDIA@XIDIAN - Xidian University)*

P.O. Box 191, No.2 South Tabai Road, 710071 Xi'an, Shaanxi Province - China

E-mail: [paolo.rocca@xidian.edu.cn](mailto:paolo.rocca@xidian.edu.cn)

Website: [www.eledia.org/eledia-xidian](http://www.eledia.org/eledia-xidian)

<sup>(3)</sup> *ELEDIA Research Center (ELEDIA@UESTC - UESTC)*

School of Electronic Engineering, Chengdu 611731 - China

E-mail: [andrea.massa@uestc.edu.cn](mailto:andrea.massa@uestc.edu.cn)

Website: [www.eledia.org/eledia-uestc](http://www.eledia.org/eledia-uestc)

<sup>(4)</sup> *Andrew Electromagnetics Laboratory - University of Illinois Chicago*

Department of Electrical and Computer Engineering, 851 South Morgan Street, Chicago, IL 60607-7053 - USA

E-mail: [derric1@uic.edu](mailto:derric1@uic.edu)

Website: <https://andrew.lab.uic.edu/>

<sup>(5)</sup> *ELEDIA Research Center (ELEDIA@TSINGHUA - Tsinghua University)*

30 Shuangqing Rd, 100084 Haidian, Beijing - China

E-mail: [andrea.massa@tsinghua.edu.cn](mailto:andrea.massa@tsinghua.edu.cn)

Website: [www.eledia.org/eledia-tsinghua](http://www.eledia.org/eledia-tsinghua)

***This work has been submitted to the IEEE for possible publication. Copyright may be transferred without notice, after which this version may no longer be accessible.***

# Multi-Scale Single-Bit *RP-EMS* Synthesis for Advanced Propagation Manipulation through System-by-Design

G. Oliveri, P. Rocca, M. Salucci, D. Erricolo, and A. Massa

## Abstract

A new method for synthesizing *Single-Bit Reconfigurable Passive Electromagnetic Skins (IRP-EMSs)* featuring advanced beam shaping capabilities is proposed. By using single-bit unit cells, the multi-scale problem of controlling *IRP-EMSs* is formulated as a two-phase process. First, the macro-scale synthesis of the discrete surface current that radiates the electromagnetic (*EM*) field fitting user-designed requirements is performed by means of an innovative quantized version of the iterative projection method (*QIPM*). Successively, the meta-atom states of the *IRP-EMS* are optimized with a customized implementation of the *System-by-Design* paradigm to yield a *IRP-EMS* that supports such a feasible reference current. A representative set of numerical results is reported to assess the effectiveness of the proposed approach in designing and controlling single-bit meta-atom *RP-EMSs* that enable complex wave manipulations.

**Key words:** Reconfigurable *EM* Skins; *EM* Holography; Reconfigurable Intelligent Surfaces; Next-Generation Communications; Iterative Projection Method; System-by-Design; Metamaterials.

# 1 Introduction and Rationale

*Electromagnetic Skins (EMSs)* are currently the core of a theoretical, methodological, and practical revolution within the academic and industrial communities working on wireless communications [1]-[10]. Several research studies on the foundation, the modeling, the simulation, the design, and the test of *EMSs* are currently under development with a strong interdisciplinary effort combining chemistry, physics, metamaterial science, electromagnetic (*EM*) engineering, telecommunications, and signal processing expertises [1]-[3][7][8]. As a matter of fact, starting from their early conceptualization as thin metasurfaces able to manipulate the wave propagation beyond Snell's laws [11], *EMSs* are considered as one of the key enabling factors of the revolutionary *Smart EM Environment (SEME)* paradigm in wireless communications [4]-[6][12][13]. Certainly, a multiplicity of methodological and practical challenges [2]-[4][8][10][11][14] still needs to be addressed to have a full transition from traditional wireless systems to the *SEME*-enhanced ones. In particular, the *complexity* associated to the design, the fabrication, the implementation, the control, and the integration within a wireless scenario of *EMSs* is the main critical issue. More specifically, complexity arises at (i) the *EMS* design level owing to the multi-scale nature of its layout that features micro/nano-scale descriptors combined with meso/macro-scale reflection and communication properties, (ii) the *SEME* level due to the interactions between the *EMSs* and the large-scale propagation scenario, and (iii) the "propagation management" level because of the need to fruitfully integrate the *EMSs* in a heterogenous wireless infrastructure, which includes the base stations, the integrated access and backhaul (*IAB*) nodes, and the smart repeaters, as well, to yield measurable performance improvements in the overall wireless network.

Within such a framework, the design of planar artificial materials with advanced propagation management capabilities has been recently demonstrated for *static passive EM skins (SP-EMS)* by exploiting artificial intelligence (*AI*) techniques within the *System-by-Design (SbD)* paradigm [5][6][15]. Such an approach leverages on the decomposition of the problem at hand into a source design phase and a subsequent optimization of the surface descriptors of the *SP-EMS* within the *Generalized Sheet Transition Condition (GSTC)* framework [5][6][11]. Thanks to the modularity of such a synthesis tool and its multi-scale-oriented nature, the efficient de-

sign of wide-aperture *EMSs* that enable advanced pattern shaping properties has been carried out [5][6] despite the use of extremely simple unit cells.

Otherwise, *reconfigurable passive EMSs (RP-EMSs)* have been proposed and widely studied to dynamically control the propagation environment for adaptively improving the communication performance [1]-[3][7][16]. Towards this end, *RP-EMS* unit cells need either analog (e.g., varactors/varistor [9][14][17] and mechanically-tuned sub-parts [10]) or digitally-controlled (e.g., p-i-n diodes [18]) components. From an applicative viewpoint, the implementation of a continuous control on each *RP-EMS* cell can yield to very expensive and complex architectures, thus it is generally avoided [19] and the *RP-EMS* analog states are often discretized using few bits,  $B$ , per cell [9][19] or they are implemented by using binary switches [18]. Therefore, *RP-EMSs* are usually digitally-controlled systems [18]-[20] with relatively limited per-cell degrees-of-freedom (*DoFs*) when compared to *SP-EMSs* [5][6]. A key consequence of such a per-cell constraint, mainly when low-bit ( $B \rightarrow 1$ ) *RP-EMS* are at hand [19], turns out to be the very limited control of the shape of the reflected beam [19]. Thus, the mainstream state-of-the-art literature on *RP-EMSs* has been concerned with the synthesis of *RP-EMSs* with “simple” anomalous reflection capabilities and narrow beam focusing (i.e., pencil beam-like) [9][18]-[20]. However, demonstrating more advanced footprint control/shaping with a digital *RP-EMS* would be of great interest in practice since it would allow one to efficiently concentrate the reflected power in arbitrary desired areas (i.e., roads, squares, streets, buildings) and not just in spots. Unfortunately, the approach derived in [5][6] to design *SP-EMSs* affording shaped footprint patterns cannot be directly applied to *RP-EMSs* [5][6]. Indeed, the synthesis of the reference surface current, which is performed in the first step of [5][6] and that exploits the non-uniqueness of the associated inverse source (*IS*) problem to take advantage of the *non-radiating currents (NRCs)* [5][21], assumes that the unit cell of the corresponding *EMS* allows a fine tuning of the reflection phase [5][6]. By definition, this is actually prevented when dealing with digital *RP-EMSs* [19] making the design process ineffective and potentially unable to fulfil complex coverage requirements.

Dealing with *RP-EMSs*, the objective of this work is twofold. On the one hand, it is aimed at presenting and validating an innovative method for the synthesis (i.e., the design and the

control) of high-performance holographic *IRP-EMS*s. On the other hand, it is devoted to prove that minimum complexity *RP-EMS*s can be used in *SEME* scenarios to yield complex wave propagation phenomena despite the coarse tuning of the reflection phase.

Starting from the design of a meta-atom of the *RP-EMS* that features only a single-bit reconfiguration and by generalizing the theoretical concepts on complex large-scale *EM* wave manipulation systems [5][6][22]-[25], the first step of the proposed method for the synthesis of *IRP-EMS*s deals with the computation of a discrete-phase current that radiates a field distribution fitting complex footprint patterns. A digital *SbD*-based *RP-EMS* optimization is then carried out to set the *IRP-EMS* configuration that supports such a reference discrete-phase current. Towards this end, suitable *AI* paradigms for building reliable and computationally-efficient “*RP-EMS* digital twins” [5][6][22]-[25] are exploited to properly address the issues related to the multi-scale complexity of the problem at hand.

The outline of the paper is as follows. First, the *IRP-EMS* synthesis problem is formulated (Sect. 2), then Sect. 3 details the proposed two-step (i.e., design and control) synthesis method. Representative results from a wide set of numerical experiments are reported for assessment purposes, while comparisons with state-of-the-art techniques [5][6] are considered (Sect. 4). Finally, some concluding remarks follow (Sect. 5).

## 2 Mathematical Formulation

Let a single-bit *RP-EMS* (*IRP-EMS*) be centered in the origin of the local coordinate system  $(x, y, z)$  (Fig. 1). The *IRP-EMS* consists of  $M \times N$  reconfigurable binary meta-atoms displaced on a regular grid of cells with sides  $\Delta x$  and  $\Delta y$  on a planar region  $\Psi_{EMS}$  ( $\Psi_{EMS} = \{-M \times \frac{\Delta x}{2} \leq x \leq M \times \frac{\Delta x}{2}; -N \times \frac{\Delta y}{2} \leq y \leq N \times \frac{\Delta y}{2}\}$ ). Each  $(m, n)$ -th ( $m = 1, \dots, M; n = 1, \dots, N$ ) meta-atom is defined by a set of  $U$  geometrical/material descriptors  $\mathbf{g} \triangleq \{g^{(u)}; u = 1, \dots, U\}$  and it features, at the  $t$ -th ( $t = 1, \dots, T$ ) time step, a binary state  $s_{mn}(t) \in \{0, 1\}$ .

The *IRP-EMS* at the  $t$ -th ( $t = 1, \dots, T$ ) instant can be univocally identified by the binary *micro-scale* state vector  $\mathcal{S}(t)$ ,  $\mathcal{S}(t) \triangleq \{s_{mn}(t); m = 1, \dots, M; n = 1, \dots, N\}$ , and the time-independent (i.e., it is unrealistic to change the atom layout at each time step) *micro-scale* descriptor vector  $\mathbf{g}$ . Otherwise, the *RP-EMS* can be described from an electromagnetic view-

point by the *micro-scale* electric/magnetic surface susceptibility vector  $\mathcal{K}(t)$  ( $t = 1, \dots, T$ ) [5][11], whose  $(m, n)$ -th entry ( $m = 1, \dots, M$ ;  $n = 1, \dots, N$ ) is the diagonal tensor of the electric/magnetic local surface susceptibility of the  $(m, n)$ -th meta-atom,  $\overline{\overline{K}}_{mn}(t)$  [ $\overline{\overline{K}}_{mn}(t) = \mathbb{K}\{\mathbf{g}; s_{mn}(t)\}$  being  $\overline{\overline{K}}_{mn}(t) \triangleq \sum_{q=x,y,z} k_{qq}(\mathbf{g}; s_{mn}(t)) \widehat{q}\widehat{q}$ ].

According to the *Generalized Sheet Transition Condition (GSTC)* technique [11][26][27], the instantaneous far field pattern,  $\overline{E}(r, \theta, \varphi; t)$ , reflected by the *RP-EMS* when illuminated by a time-harmonic plane wave at frequency  $f$  impinging from the incidence direction  $(\theta^{inc}, \varphi^{inc})$  and characterized by “perpendicular” and “parallel” complex-valued electric field components  $E_{\perp}^{inc}$  and  $E_{\parallel}^{inc}$  is a function of the surface susceptibility vector  $\mathcal{K}$  through the *macro-scale* induced surface current  $\overline{J}$  (i.e.,  $\overline{E}(r, \theta, \varphi; t) = \mathbb{F}\{\overline{J}(x, y; t)\}$ ). More in detail, it turns out to that [5][6][11][32]

$$\begin{aligned} \overline{E}(r, \theta, \varphi; t) = & \frac{jk_0 \exp(-jk_0 r)}{4\pi r} \int_{-\frac{M\Delta x}{2}}^{\frac{M\Delta x}{2}} \int_{-\frac{N\Delta y}{2}}^{\frac{N\Delta y}{2}} \overline{J}(x', y'; t) \times \\ & \exp[jk_0(r x' \sin \theta \cos \varphi + r y' \sin \theta \sin \varphi)] dx' dy' \end{aligned} \quad (1)$$

where the surface current  $\overline{J}$  is given by

$$\overline{J}(x, y; t) = \widehat{\mathbf{r}} \times \left[ \eta_0 \widehat{\mathbf{r}} \times \overline{J}^e(x, y; t) + \overline{J}^h(x, y; t) \right] \quad (x, y) \in \Psi_{EMS} \quad (2)$$

where  $\overline{J}^o$ ,  $o \in \{e, h\}$ , is the electric/magnetic component of the current induced on the *RP-EMS*, while  $k_0 = 2\pi f \sqrt{\varepsilon_0 \mu_0}$  and  $\eta_0 = \sqrt{\frac{\mu_0}{\varepsilon_0}}$  are the free-space wavenumber and the impedance, respectively, which depend on the free-space permeability (permittivity)  $\mu_0$  ( $\varepsilon_0$ ).

Subject to the local periodicity condition, the dependence of  $\overline{J}^o$ ,  $o \in \{e, h\}$ , on the entries of the *micro-scale* electric/magnetic surface susceptibility vector  $\mathcal{K}$  (i.e.,  $\overline{J}^o(x, y; t) = \mathbb{G}\{\mathbb{K}^o\{\mathbf{g}; s_{mn}(t)\}; \overline{E}^{inc}(x, y, 0; t)\}$ ,  $o \in \{e, h\}$ ) is made explicit in the following form [5][6][11][27]

$$\begin{aligned} \overline{J}^e(x, y; t) = & \sum_{m=1}^M \sum_{n=1}^N \left\{ j2\pi f \varepsilon_0 \left[ \overline{\overline{K}}_{mn}^e(t) \cdot \overline{E}_{mn}(t) \right]_{\tau} - \widehat{\nu} \times \nabla_{\tau} \left[ \overline{\overline{K}}_{mn}^h(t) \cdot \overline{H}_{mn}(t) \right]_{\nu} \right\} \Omega_{mn}(x, y) \\ \overline{J}^h(x, y; t) = & \sum_{m=1}^M \sum_{n=1}^N \left\{ j2\pi f \mu_0 \left[ \overline{\overline{K}}_{mn}^h(t) \cdot \overline{H}_{mn}(t) \right]_{\tau} + \widehat{\nu} \times \nabla_{\tau} \left[ \overline{\overline{K}}_{mn}^e(t) \cdot \overline{E}_{mn}(t) \right]_{\nu} \right\} \Omega_{mn}(x, y) \end{aligned} \quad (3)$$

where  $\widehat{\nu}$  is the outward normal to  $\Psi_{EMS}$ ,  $[\cdot]_{\tau/\nu}$  stands for the tangential/normal component, and  $\Omega_{mn}(x, y) \triangleq \{1 \text{ if } [-(m-M-1) \times \frac{\Delta x}{2} \leq x \leq (m-M) \times \frac{\Delta x}{2}] \text{ and } [-(n-N-1) \times -\frac{\Delta y}{2}$

$\leq y \leq (n - N) \times \frac{\Delta y}{2}$ ; 0 otherwise} is the basis function related to the  $(m, n)$ -th ( $m = 1, \dots, M$ ;  $n = 1, \dots, N$ ) cell with support  $\Delta\Psi_{EMS}$  ( $\Delta\Psi_{EMS} \triangleq \Delta x \times \Delta y$ ), while  $\overline{E}_{mn}$  ( $\overline{H}_{mn}$ ) is the surface averaged electric (magnetic) field (see *Appendix*).

Such a derivation points out that the  $t$ -th ( $t = 1, \dots, T$ ) far-field pattern  $\overline{E}(r, \theta, \varphi; t)$  can be controlled by properly adjusting the  $M \times N$  binary entries of  $\mathcal{S}(t)$ , once the *IRP-EMS* is designed (i.e.,  $\mathbf{g}$  is set - Sect. 2.1). Accordingly, the problem at hand can be mathematically formulated as follows

***IRP-EMS Synthesis Problem*** - Find the optimal setting of the micro-scale descriptor vector,  $\mathbf{g}^{opt}$ , and the optimal configuration of  $T$  binary *micro-scale* state vectors,  $\{\mathcal{S}^{opt}(t); t = 1, \dots, T\}$ , such that

$$\Phi(\mathbf{g}, \mathcal{S}(t)) = \int_{\Psi_{obs}} \Re \{ F^{des}(\tilde{x}, \tilde{y}, \tilde{z}; t) - F(\tilde{x}, \tilde{y}, \tilde{z}; t) \} d\tilde{x}d\tilde{y}d\tilde{z} \quad (4)$$

is minimized at each  $t$ -th ( $t = 1, \dots, T$ ) time instant [i.e.,  $(\mathbf{g}^{opt}, \mathcal{S}^{opt}(t)) = \arg(\min_{\mathbf{g}, \mathcal{S}(t)} [\Phi(\mathbf{g}, \mathcal{S}(t))])$ ,  $t = 1, \dots, T$ ].

In (4),  $\Re \{ . \}$  is the ‘‘ramp’’ function and  $F^{des}(\tilde{x}, \tilde{y}, \tilde{z}; t)$  is the user-defined power pattern footprint at the  $t$ -th ( $t = 1, \dots, T$ ) time instant in the observation region  $\Psi_{obs}$ ,  $(\tilde{x}, \tilde{y}, \tilde{z})$  being the *RP-EMS* global coordinate system (Fig. 1). Moreover, the footprint pattern is a function of the reflected far-field pattern  $\overline{E}(r, \theta, \varphi; t)$ , (i.e.,  $F(\tilde{x}, \tilde{y}, \tilde{z}; t) = \Re \{ \overline{E}(r, \theta, \varphi; t) \}$ ) and it is given by

$$F(\tilde{x}, \tilde{y}, \tilde{z}; t) = \left| \overline{E} \left( \sqrt{\tilde{x}^2 + \tilde{y}^2 + (\tilde{z} - d)^2}, \arctan \frac{\sqrt{\tilde{y}^2 + (\tilde{z} - d)^2}}{\tilde{x}}, \arctan \left( \frac{\tilde{z} - d}{\tilde{x}} \right); t \right) \right|^2 \quad (5)$$

where  $d$  is the *IRP-EMS* height over the ground plane (Fig. 1).

It is worth noticing that, unlike the case of *SP-EMSs*, the synthesis of a *IRP-EMS* cannot be done by minimizing (4) only once since there is a different optimal configuration  $\mathcal{S}^{opt}(t)$  for each  $t$ -th ( $t = 1, \dots, T$ ) user-defined footprint pattern,  $F^{des}(\tilde{x}, \tilde{y}, \tilde{z}; t)$ , as pointed out in the following expression

$$\Phi(\mathbf{g}, \mathcal{S}(t)) = \int_{\Psi_{obs}} \Re \left\{ F^{des}(\tilde{x}, \tilde{y}, \tilde{z}; t) - \Re \left\{ \mathbb{F} \left\{ \mathbb{G} \left\{ \mathbb{K} \{ \mathbf{g}; s_{mn}(t) \}; \overline{E}^{inc}(x, y, 0; t) \right\} \right\} \right\} \right\} d\tilde{x}d\tilde{y}d\tilde{z} \quad (6)$$

where the link between  $F^{des}(\tilde{x}, \tilde{y}, \tilde{z}; t)$  and  $\mathcal{S}(t) \triangleq \{s_{mn}(t); m = 1, \dots, M; n = 1, \dots, N\}$  is made evident. On the other hand, the  $U$  geometrical/material entries of  $\mathbf{g}^{opt}$  must be set once as the optimal trade-off among all  $T$  propagation scenarios.

Furthermore, the problem at hand is more complex than that of a multi-bit *RP-EMS* and (even) much more than of a *SP-EMS*. Unlike the *SP* case, the  $t$ -th ( $t = 1, \dots, T$ ) *micro-scale* electric/magnetic surface susceptibility vector  $\mathcal{K}(t)$  assumes here only a quantized set of states (i.e.,  $2^{M \times N}$ ) instead of a continuity of values [5][6]. Thus, the macro-scale (reflection) properties of the arising *EMS* turn out to be more severely constrained than those of a *SP-EMS* or a multi-bit *RP-EMS*. Consequently, the fulfilment of complex shaping requirements on the footprint power pattern, as those in [5][6], is certainly more difficult and it may results even physically unfeasible.

Taking into account these considerations, the “*IRP-EMS Synthesis Problem*” (4) is then addressed with a two-step approach where, first, the “*IRP-EMS Design Problem*” (Sect. 2.1) is solved by identifying the  $U$  geometrical/material descriptors of the single-bit meta-atom (i.e.,  $\mathbf{g} \leftarrow \mathbf{g}^{opt}$ ), while the second step is aimed at setting, at each  $t$ -th ( $t = 1, \dots, T$ ) time-instant, the entries of the *micro-scale* state vector  $\mathcal{S}(t)$  to fulfil the footprint pattern requirements [i.e.,  $\mathcal{S}(t) \leftarrow \mathcal{S}^{opt}(t)$ ] (“*IRP-EMS Control Problem*” - Sect. 2.2).

## 2.1 *IRP-EMS* Design Problem

As for the *IRP-EMS* unit cell design, a key challenge and preparatory step to enable the footprint pattern control (i.e.,  $F \rightarrow F^{des}$ ) is the choice of a meta-atom structure whose reflection properties can be suitably modified when its logical state is changed [11]. In principle, an optimal trade-off should be found by minimizing (6) with respect to  $\mathbf{g}$  across all  $T$  user-requirements  $\{F^{des}(\tilde{x}, \tilde{y}, \tilde{z}; t); t = 1, \dots, T\}$ , while, in this paper, a “worst case”-strategy is adopted to yield a more general and flexible implementation. The design is then carried out by requiring that the *IRP-EMS* meta-atom supports the widest possible reflection variation to account not only the  $T$  propagation scenarios at hand, but more in general the largest range of admissible conditions. According to (3), such a guideline corresponds to the maximization of the gap between the values of the electric/magnetic local surface susceptibility when switching the status of the



generic  $(m, n)$ -th ( $m = 1, \dots, M; n = 1, \dots, N$ ) meta-atom from  $s_{mn}(t) = 0$  to  $s_{mn}(t) = 1$ .

Mathematically, this means to minimize the following cost function

$$\begin{aligned} \phi(\mathbf{g}) = & \frac{1}{\pi^2} \left[ \left( \left| \angle \Gamma_{mn}^{\perp\perp}(t) \Big|_{f=f_0}^{s_{mn}(t)=1} - \angle \Gamma_{mn}^{\perp\perp}(t) \Big|_{f=f_0}^{s_{mn}(t)=0} \right| - \pi \right)^2 + \right. \\ & \left. + \left( \left| \Gamma_{mn}^{\parallel\parallel}(t) \Big|_{f=f_0}^{s_{mn}(t)=1} - \Gamma_{mn}^{\parallel\parallel}(t) \Big|_{f=f_0}^{s_{mn}(t)=0} \right| - \pi \right)^2 \right] \end{aligned} \quad (7)$$

to yield the optimal set of the geometrical/material descriptors of the single-bit meta-atom,  $\mathbf{g}^{opt}$  [i.e.,  $\mathbf{g}^{opt} = \arg(\min_{\mathbf{g}} [\phi(\mathbf{g})])$ ]. In (7),  $f_0$  is the central working frequency,  $\angle \cdot$  stands for the phase of the complex argument, and  $\Gamma_{mn}^{\perp\perp}(t) / \Gamma_{mn}^{\parallel\parallel}(t)$  [ $\Gamma_{mn}^{\perp\perp}(t) = \mathbb{Y}^{\perp\perp} \{\mathbf{g}; s_{mn}(t)\}$  and  $\Gamma_{mn}^{\parallel\parallel}(t) = \mathbb{Y}^{\parallel\parallel} \{\mathbf{g}; s_{mn}(t)\}$ ] are the *TE/TM* co-polar components of the reflection tensor in the  $(m, n)$ -th ( $m = 1, \dots, M; n = 1, \dots, N$ ) cell,  $\overline{\Gamma}_{mn}(t)$ , while the logical status of the  $(m, n)$ -th cell (i.e.,  $s_{mn}(t) \in \{0, 1\}$ ) is physically implemented by biasing the diodes in the meta-atom layout (Fig. 2).

## 2.2 IRP-EMS Control Problem

Once the *IRP-EMS* has been designed by setting  $\mathbf{g}^{opt}$ , the computation of  $\mathcal{S}^{opt}(t)$  should be performed by minimizing the constrained ( $\mathbf{g} \equiv \mathbf{g}^{opt}$ ) version of (4)

$$\Phi(\mathbf{g}^{opt}, \mathcal{S}(t)) = \int_{\Psi_{obs}} \Re \left\{ F^{des}(\tilde{x}, \tilde{y}, \tilde{z}; t) - \mathbb{H} \left\{ \mathbb{F} \left\{ \mathbb{G} \left\{ \mathbb{K} \left\{ \mathbf{g}^{opt}; s_{mn}(t) \right\}; \overline{E}^{inc}(x, y, 0; t) \right\} \right\} \right\} \right\} d\tilde{x}d\tilde{y}d\tilde{z} \quad (8)$$

[i.e.,  $\mathcal{S}^{opt}(t) = \arg(\min_{\mathcal{S}} [\Phi(\mathbf{g}^{opt}, \mathcal{S}(t))])$ ], which directly relates the state vector  $\mathcal{S}(t)$  with the footprint target  $F^{des}(\tilde{x}, \tilde{y}, \tilde{z}; t)$ . However, when dealing with *aperiodic* wave manipulation devices [5][28]-[31], such a single-phase solution approach is usually avoided in favour of splitting the problem at hand into two parts. The former phase (“*Reference Current Computation*”) addresses a *macro-scale* objective that consists in the computation of an ideal equivalent surface current  $\overline{J}^{opt}(x, y; t)$  that affords the desired footprint pattern  $F^{des}(\tilde{x}, \tilde{y}, \tilde{z}; t)$ , which is coded into the following macro-scale cost function

$$\Phi(\overline{J}(x, y; t)) = \int_{\Psi_{obs}} \Re \left\{ F^{des}(\tilde{x}, \tilde{y}, \tilde{z}; t) - \mathbb{H} \left\{ \mathbb{F} \left\{ \overline{J}(x, y; t) \right\} \right\} \right\} d\tilde{x}d\tilde{y}d\tilde{z}, \quad (9)$$

to be minimized

$$\overline{\mathcal{J}}^{opt}(x, y; t) = \arg \left( \min_{\overline{\mathcal{J}}(x, y)} [\Phi(\overline{\mathcal{J}}(x, y; t))] \right). \quad (10)$$

The second (*microscale*) phase (“*IRP-EMS Configuration*”) [5][28]-[31] is devoted to choose the meta-atoms configuration  $\mathcal{S}^{opt}(t)$  that supports the reference current  $\overline{\mathcal{J}}^{opt}(x, y; t)$  by solving the following optimization problem

$$\mathcal{S}^{opt}(t) = \arg \left( \min_{\mathcal{S}} [\psi(\mathcal{S}(t))] \right), \quad (11)$$

where

$$\psi(\mathcal{S}(t)) \triangleq \frac{\left\| \overline{\mathcal{J}}^{opt}(x, y; t) - \mathbb{G} \left\{ \mathbb{K} \{ \mathbf{g}; s_{mn}(t) \}; \overline{E}^{inc}(x, y, 0; t) \right\} \right\|}{\left\| \overline{\mathcal{J}}^{opt}(x, y; t) \right\|}. \quad (12)$$

This two-phase process exploits the fast Fourier relation between currents and patterns (1), which results in very efficient implementations for large apertures [5][28]-[31], as well. Moreover, the arising currents can be re-used to design *EMS* arrangements with different unit cells [31]. Furthermore, the micro-scale synthesis step does not involve here the optimization of  $\overline{\overline{K}}_{mn}$  to achieve ideal susceptibility distributions (which may yield, even in the *SP-EMS* case [5][6], to non-feasible anisotropy requirements on the cell), but it is aimed at setting the  $(m, n)$ -th ( $m = 1, \dots, M; n = 1, \dots, N$ ) atom state  $s_{mn}(t)$  that locally minimizes the mismatch with the target surface current.

On the other hand, it has to be noticed that in principle the problem at hand, whatever the solution approach (direct or two-phases), requires the phase of the wave reflected by the meta-atoms to vary over continuous intervals [5][28]-[31]. This is clearly not true when dealing with  $B$ -bits *RP-EMSs*, since each meta-atom can only assume  $2^B$  states for each  $t$ -th ( $t = 1, \dots, T$ ) time instant. Such a limitation is even more critical for *IRP-EMSs* ( $B = 1$ ). Moreover, despite the two-phase decomposition, the multi-scale and quantized nature of the *IRP-EMS Control Problem* still yields to a solution space with a size (i.e.,  $2^{M \times N}$ ) that grows exponentially with the *RP-EMS* aperture.

To take into account these pros & cons, a dedicated strategy needs to be implemented (Sect. 3).

### 3 Solution Method

While the “*IRP-EMS Design*” problem (Sect. 2.1) is a quite standard real-variable optimization problem to be addressed with a standard optimization tool, the “*IRP-EMS Control*” one (Sect. 2.2) turns out to be a new challenge. As a matter of fact, the most intuitive strategy for solving this latter would be that of exploiting the methodology discussed in [5] by simply replacing the model of the local susceptibility dyadics of the *SP-EMS* with that of the reconfigurable single-bit meta-atom at hand. However, such an approach has a fundamental drawback when applied to the *IRP-EMS* control. By ignoring the quantized nature of the *IRP-EMS* surface currents in the “*Reference Current Computation*” (10), there may not to be an implementable current distribution,  $\bar{\mathcal{J}}(\bar{\mathcal{J}}(x, y; t) = \mathbb{G} \left\{ \mathbb{K} \{ \mathbf{g}; s_{mn}(t) \}; \bar{E}^{inc}(x, y, 0; t) \right\})$ , that approximates the synthesized reference current  $\bar{\mathcal{J}}^{opt}$ , regardless of the approach to configure the *IRP-EMS* (11). Therefore, an innovative method is proposed (Sect. 3.1) to compute a “feasible” ideal equivalent surface current  $\bar{\mathcal{J}}^{opt}$  that affords the desired footprint pattern  $F^{des}$ , while the approach used in [5] for the design of an *SP-EMS* is customized here to control the *IRP-EMS* (3.2).

#### 3.1 QIPM-Based Reference Current Computation

In order to define a “feasible” reference current, a quantized version of the iterative projection method (*QIPM*) is derived.

Let  $\mathcal{C}$  be the “*IRP-EMS Current Space*” composed by the whole set of the *IRP-EMS* admissible surface currents having the following mathematical form

$$\bar{\mathcal{J}}(x, y; t) = \sum_{m=1}^M \sum_{n=1}^N \alpha_{mn}(t) \exp[j\chi_{mn}(t)] \Omega_{mn}(x, y) \hat{t} \quad (13)$$

where  $\hat{t}$  denotes the current polarization, while  $\alpha_{mn}(t)$  [ $\alpha_{mn}(t) = \mathbb{A} \{ s_{mn}(t) \}$ ] and  $\chi_{mn}(t)$  [ $\chi_{mn}(t) = \mathbb{X} \{ s_{mn}(t) \}$ ] are the values of the locally-controlled magnitude and phase of the surface current that belong to the discrete (two-elements) alphabets  $\mathcal{A}$  and  $\mathcal{X}$ , respectively. The elements of  $\mathcal{A}$  and  $\mathcal{X}$  are the magnitude and the phase of the current that each meta-atom can support when configured in one of its binary states,  $s_{mn}(t) \in \{0, 1\}$ , ( $\mathcal{A} \triangleq \{ \mathbb{A} \{ s_{mn}(t) = 0 \}, \mathbb{A} \{ s_{mn}(t) = 1 \} \}$  and  $\mathcal{X} \triangleq \{ \mathbb{X} \{ s_{mn}(t) = 0 \}, \mathbb{X} \{ s_{mn}(t) = 1 \} \}$ ).

Starting from a random initialization of the discrete coefficients  $\alpha_{mn}^{(p)}(t)$  and  $\chi_{mn}^{(p)}(t)$  ( $m = 1, \dots, M; n = 1, \dots, N$ ), whose values are randomly drawn from  $\mathcal{A}$  and  $\mathcal{X}$ , the *QIPM* generates a succession of  $P$  trial current distributions,  $\{\bar{\mathcal{J}}^{(p)}; p = 1, \dots, P\}$ . First, the footprint pattern  $F^{(p)}(\tilde{x}, \tilde{y}, \tilde{z}; t)$  afforded by  $\bar{\mathcal{J}}^{(p)}$  is computed (1)(5). It is then projected into the corresponding feasibility space through the projection operator  $R^{(p)}$  [ $R^{(p)}(\tilde{x}, \tilde{y}, \tilde{z}; t) = \mathbb{R}\{F^{(p)}(\tilde{x}, \tilde{y}, \tilde{z}; t), F^{des}(\tilde{x}, \tilde{y}, \tilde{z}; t)\}$ ]

$$R^{(p)}(\tilde{x}, \tilde{y}, \tilde{z}; t) = \begin{cases} F^{des}(\tilde{x}, \tilde{y}, \tilde{z}; t) & \text{if } F^{(p)}(\tilde{x}, \tilde{y}, \tilde{z}; t) < F^{des}(\tilde{x}, \tilde{y}, \tilde{z}; t) \\ F^{(p)}(\tilde{x}, \tilde{y}, \tilde{z}; t) & \text{otherwise.} \end{cases} \quad (14)$$

The *QIPM* convergence is checked and the iterations are stopped if either  $p = P$  or if the index  $\Xi^{(p)}(t)$  ( $\Xi^{(p)}(t) \triangleq \frac{\int_{\Psi_{obs}} |R^{(p)}(\tilde{x}, \tilde{y}, \tilde{z}; t) - F^{(p)}(\tilde{x}, \tilde{y}, \tilde{z}; t)| d\tilde{x}d\tilde{y}d\tilde{z}}{\int_{\Psi_{obs}} |F^{(p)}(\tilde{x}, \tilde{y}, \tilde{z}; t)| d\tilde{x}d\tilde{y}d\tilde{z}}$ ) complies with the convergence condition  $\Xi^{(p)}(t) \leq \Xi^{th}$ . If this holds true, the reference current is set to the  $p$ -th estimate,  $\bar{\mathcal{J}}^{opt} = \bar{\mathcal{J}}^{(p)}$ . Otherwise, the minimum norm current,  $\bar{\mathcal{J}}_{MN}^{(p)}$ , corresponding to  $R^{(p)}(\tilde{x}, \tilde{y}, \tilde{z}; t)$  is retrieved by means of the truncated singular value decomposition [5][21]

$$\bar{\mathcal{J}}_{MN}^{(p)} = \mathbb{F}^{-1} \{ \mathbb{H}^{-1} \{ R^{(p)}(\tilde{x}, \tilde{y}, \tilde{z}; t) \} \}. \quad (15)$$

The quantization of the minimum norm current is subsequently carried out by approximating it with the closest element of  $\mathcal{C}$  ( $\bar{\mathcal{J}}^{(p+1)} \approx \bar{\mathcal{J}}_{MN}^{(p)}, \bar{\mathcal{J}}^{(p+1)} \in \mathcal{C}$ ). More in detail, the amplitude and the phase coefficients of  $\bar{\mathcal{J}}^{(p+1)}$  are determined by minimizing the mismatch cost function

$$\rho(\alpha_{mn}(t), \chi_{mn}(t)) = \left\{ \frac{\left\| \sum_{m=1}^M \sum_{n=1}^N \alpha_{mn}(t) \exp[j\chi_{mn}(t)] \Omega_{mn}(x, y) \hat{t} - \bar{\mathcal{J}}_{MN}^{(p)} \right\|^2}{\left\| \bar{\mathcal{J}}_{MN}^{(p)} \right\|^2} \right\} \quad (16)$$

$\|\cdot\|$  being the  $\ell_2$  norm [i.e.,  $(\alpha_{mn}^{(p+1)}(t), \chi_{mn}^{(p+1)}(t)) = \arg \min_{\substack{\alpha_{mn}(t) \in \mathcal{A} \\ \chi_{mn}(t) \in \mathcal{X}}} \{\rho(\alpha_{mn}(t), \chi_{mn}(t))\}$ ], they are then substituted in (13) to yield  $\bar{\mathcal{J}}^{(p+1)}$ . The iteration index is then updated ( $p \leftarrow p + 1$ ) and the entire *QIPM* process is restarted from the footprint pattern computation.

It is worth pointing out that, unlike state-of-the-art approaches [5][6], the operation in (16) outputs an estimated current  $\bar{\mathcal{J}}^{(p+1)}$  that fulfils the feasibility condition, thus it is assured that the current distribution determined at the convergence,  $\bar{\mathcal{J}}^{opt}$ , can be surely implemented with a *IRP-EMS* layout.

### 3.2 IRP-EMS Configuration Method

By following the guidelines in [5], but here customized to a binary control problem, a *SbD*-based optimization is carried out to identify the *IRP-EMS* discrete micro-scale status  $\mathcal{S}^{opt}(t)$  of  $M \times N$  binary entries. Towards this end, a set of  $L$  trial *IRP-EMS* configurations

$$\langle \mathcal{S}(t) \rangle \triangleq \{\mathcal{S}_l(t); l = 1, \dots, L\} \quad (17)$$

is iteratively processed until either the number of *SbD* iterations reaches the maximum value  $I$  ( $i = I$ ,  $i$  being the iteration index) or the feasible reference current distribution  $\bar{\mathcal{J}}^{opt}$ , computed in Sect. 3.1, is matched (12) [i.e.,  $\psi(\mathcal{S}^{opt}(t)) \leq \psi^{th}$ ,  $\mathcal{S}^{opt}(t) = \arg\left(\min_{l,i} \left[\psi\left(\mathcal{S}_l^{(i)}(t)\right)\right]\right)$ ,  $\psi^{th}$  being a user-defined convergence threshold].

Starting from a random initial configuration,  $\langle \mathcal{S}^{(i)}(t) \rangle_{i=0}$ , each  $i$ -th ( $i = 1, \dots, I$ ) iteration consists of the following operations:

- *IRP-EMS Surrogate Modeling* - The set of  $L$  micro-scale electric/magnetic surface susceptibility vectors,  $\langle \mathcal{K}^{(i)}(t) \rangle$  ( $\langle \mathcal{K}(t) \rangle \triangleq \{\mathcal{K}_l(t); l = 1, \dots, L\}$ ), is predicted with an *AI*-based technique, featuring an *Ordinary Kriging* implementation, according to the most recent trends in the surrogate modeling of wave manipulating devices [24][33]. For each  $l$ -th entry of  $\langle \mathcal{K}^{(i)}(t) \rangle$ , the diagonal tensor of the electric/magnetic local surface susceptibility of the  $(m, n)$ -th ( $m = 1, \dots, M; n = 1, \dots, N$ ) meta-atom,  $\overline{\overline{K}}_{mn}(t)$ , is approximated with its digital-twin (*DT*),  $\overline{\overline{K}}_{mn}(t) \approx \overline{\overline{K}}_{mn}^{DT}(t)$  ( $\overline{\overline{K}}_{mn}^{DT}(t) \triangleq \mathbb{K}^{DT}\{\mathbf{g}; s_{mn}(t)\}$ ), which is off-line trained starting from  $V$  full-wave evaluations of the meta-atom response  $\{\mathbf{g}_v, s_{mn}^v(t); \mathbb{K}\{\mathbf{g}_v; s_{mn}^v(t)\}; v = 1, \dots, V\}$  [24][33];
- *Surface Current Computation* - The distribution of the surface current  $\bar{\mathcal{J}}_l(x, y; t)$  induced on the  $l$ -th ( $l = 1, \dots, L$ ) *IRP-EMS*, which is modeled with the surrogate susceptibility vector  $\mathcal{K}_l^{DT}(t)$ , is computed by setting  $\overline{\overline{K}}_{mn}(t) = \overline{\overline{K}}_{mn}^{DT}(t)$  in (3);
- *Surface Current Fitness Evaluation* - The mismatch between  $\bar{\mathcal{J}}_l^{(i)}$  ( $l = 1, \dots, L$ ) and  $\bar{\mathcal{J}}^{opt}$  is quantified by calculating the value of the micro-scale cost function (12),  $\psi\left(\mathcal{S}_l^{(i)}(t)\right)$ ;
- *Guess Current Update* - A new set of *IRP-EMS* states,  $\langle \mathcal{S}^{(i+1)}(t) \rangle$ , is generated by ap-

plying the Genetic-Algorithm (*GA*) operators [34] to the previous guesses,  $\langle \mathcal{S}^{(i)}(t) \rangle$ , according their fitness values,  $\langle \psi^{(i)}(t) \rangle$  ( $\langle \psi^{(i)}(t) \rangle \triangleq \{\psi(\mathcal{S}_l^{(i)}(t)); l = 1, \dots, L\}$ ). Unlike [5][6], a *GA*-based optimization is performed due to the binary *DoFs* of the problem at hand.

## 4 Numerical Results

This section is aimed at illustrating the synthesis process of *IRP-EMS*s described in Sect. 3 as well as at demonstrating its effectiveness and potentialities. Towards this end, the design of the single-bit meta-atom is first presented along with the full-wave validation of its properties (Sect. 4.1). Afterwards, the *IRP-EMS* control is assessed through a selected set of numerical experiments (Sect. 4.2). For the full-wave modeling of both the meta-atom and the finite *IRP-EMS* layouts, the *Ansys HFSS* [35] *EM* simulator has been used.

### 4.1 Single-Bit Meta-Atom Design and Validation

Since a key objective of this work is to prove that it is possible to achieve advanced beam shaping properties with minimum-complexity *RP-EMS*s, the design of the single-bit meta-atom has been carried out according to Sect. 2.1 by also taking into account the following constraints: (i) the meta-atom features a single-layer geometry to minimize the fabrication complexity; (ii) the single-bit ( $B = 1$ ) reconfigurability of the *RP-EMS* unit cell is obtained by applying a single bias voltage; (iii) the shape of the layout of the printed cell is very regular to keep its *EM* behavior independent on the accuracy of the fabrication process; (iv) the *IRP-EMS* structure works whatever the polarization of the incident field.

The unit cell in [36] has been then considered as reference model. It consists of a simple square patch (Fig. 2) with two edges connected to the ground plane through two p-i-n diodes [green rectangles - Fig. 2(a)] and two vias [yellow circles - Fig. 2(a)]. By applying a bias voltage at the center of the patch, the diodes can be either both set to the “ON” [ $s_{mn}(t) = 1$ ] or both to the “OFF” [ $s_{mn}(t) = 0$ ] states to implement the single-bit-per-atom reconfigurability.

To operate at the central frequency of the sub-6GHz *n78* band [37] (i.e.,  $f_0 = 3.5$  [GHz]),

such a reference model has been tuned by considering a Rogers RO4350 ( $\varepsilon_r = 3.66$ ,  $\tan \delta = 4.0 \times 10^{-3}$ ) substrate with thickness of  $1.524 \times 10^{-3}$  [m] that includes  $3.5 \times 10^{-5}$  [m]-thick metallizations and the MACOM MADP-000907-14020 diodes. The values of the  $\mathbf{g}^{opt}$  entries are listed in Tab. I, while the CAD models of the unit cell and of the switching device are shown in Fig. 2(b) and Fig. 2(c), respectively.

The reflection performance of the optimized meta-atom are illustrated in Fig. 3 for the broadside incidence. More in detail, the plots of the phase [Fig. 3(a)] and the magnitude [Fig. 3(b)] of the  $TE/TM$  components of the local reflection tensor  $\overline{\overline{\Gamma}}_{mn}(t)$  indicate that such a meta-atom supports a  $\approx 180$  [deg] phase difference between the “ON” [ $s_{mn}(t) = 1$ ] and the “OFF” [ $s_{mn}(t) = 0$ ] states at  $f_0$  [Fig. 3(a)]. Thanks to the symmetry of the layout, the arising unit-cell is insensitive to the polarization [Fig. 3(a)]. Moreover, the losses are limited [ $< 4$  [dB] - Fig. 3(b)] and the cross-polarization level is low [ $< -18$  [dB] - Fig. 3(b)] within the whole frequency band.

It is finally worthwhile to remark that, while the successive control step (Sect. 2.2) has been performed in this paper with the single-bit cell in Fig. 2, the proposed approach for configuring the *IRP-EMS* can be adopted regardless of the working frequency, the number of bits per cell,  $B$ , and the meta-atom complexity [38].

## 4.2 Single-Bit *RP-EMS* Control

To assess the features and the potentialities of the *IRP-EMS* control method in Sects. 3.1-3.2, different *EMS* apertures and target radiation performance have been analyzed by considering a *SEME* scenario where a *IRP-EMS* is placed at  $d = 5$  [m] over the ground (Fig. 1), it is illuminated by a base station located along the *EMS* broadside direction [i.e.,  $(\theta^{inc}, \varphi^{inc}) = (0, 0)$  [deg]  $\rightarrow \hat{\mathbf{e}}_{\perp} = \hat{\mathbf{y}}$  and  $\hat{\mathbf{e}}_{\parallel} = \hat{\mathbf{x}}$ ], and it is equipped with a slant  $+45$  [deg] linearly polarized antenna (i.e.,  $E_{\perp}^{inc} = E_{\parallel}^{inc} = 1$ ). As for the calibration setup of the *IRP-EMS* control, the following values have been chosen according to the guidelines in [5][24]:  $V = 2 \times 10^4$ ,  $P = 10^2$ ,  $L = 20$ ,  $\Xi^{th} = 10^{-4}$ ,  $\psi^{th} = 10^{-3}$ , and  $I = 10^4$ .

The first experiment is aimed at configuring a  $M \times N = 10 \times 10$  *IRP-EMS* to maximize the reflected power in a square  $\Psi_{cov}$  of size  $10 \times 10$  [m<sup>2</sup>] located in the global coordinate system

(Fig. 1) at  $(\tilde{x}, \tilde{y}, \tilde{z}) = (25, 30, 0)$  [m], which corresponds to set the desired footprint pattern as follows

$$F^{des}(\tilde{x}, \tilde{y}, \tilde{z}; t) = \begin{cases} -10 \text{ [dB]} & (\tilde{x}, \tilde{y}, \tilde{z}) \in \Psi_{cov} \\ -50 \text{ [dB]} & (\tilde{x}, \tilde{y}, \tilde{z}) \notin \Psi_{cov} \end{cases} \quad (18)$$

with  $t = T = 1$ .

Figure 4(a) shows the behaviour of the macro-scale cost function (9)  $\Phi^{(p)}$  during the *QIPM*-based process ( $p = 1, \dots, P$ ) for the synthesis of the reference surface current in comparison with that of the *IPM* technique [5]. As expected, the *QIPM* does not outperform the *IPM* in terms of footprint pattern matching (i.e.,  $\Phi_{QIPM}^{(p)} > \Phi_{IPM}^{(p)}$ ,  $p = 1, \dots, P$ ) since the former is a constrained version of the latter owing to the binary nature of the meta-atoms and the quantization of the arising current distribution. Indeed, unlike the smoothly varying phase distribution of the *IPM* [Fig. 4(b)] that ignores any limitation to the phase control, the profile of the phase distribution of the *QIPM* current turns out to be binarized [Fig. 4(c)]. Such an apparent drawback [Fig. 4(a)] is actually a fundamental advantage of the *QIPM* when dealing with the subsequent *SbD*-driven micro-scale state optimization (Fig. 5). As a matter of fact, the plot of the local error  $\sigma(m, n)$  ( $m = 1, \dots, M$ ;  $n = 1, \dots, N$ )

$$\sigma(m, n; t) \triangleq \angle \bar{\mathcal{J}}^{opt}(x_m, y_n; t) - \angle \bar{\mathcal{J}}^*(x_m, y_n; t) \quad (19)$$

$[\bar{\mathcal{J}}^*(x, y; t) = \mathbb{G} \{ \mathbb{K} \{ \mathbf{g}; s_{mn}^{opt}(t) \}; \bar{\mathbf{E}}^{inc}(x, y, 0; t) \}]$  in approximating the phase of the reference current distribution with the *IRP-EMS* in Fig. 5(b) points out that it is more difficult to match the *IPM*-synthesized one, while the mismatch reduces in the *QIPM* case [Fig. 5(a)] (i.e.,  $3 \leq \sigma^{IPM}(m, n) \leq 121$  [deg] vs.  $0.2 \leq \sigma^{QIPM}(m, n) \leq 0.45$  [deg]), as one can visually notice by comparing the phase profiles of the reference and the synthesized currents  $[\bar{\mathcal{J}}_{IPM}^{opt}(x, y; t)$  - Fig. 4(b) vs.  $\bar{\mathcal{J}}_{IPM}^*(x, y; t)$  - Fig. 5(c);  $\bar{\mathcal{J}}_{QIPM}^{opt}(x, y; t)$  - Fig. 4(c) vs.  $\bar{\mathcal{J}}_{QIPM}^*(x, y; t)$  - Fig. 5(d)].

In order to analyze the impact of those results on the coverage performance, the plots of the analytically-computed [Figs. 6(c)-6(d)] and the *HFSS*-simulated [Figs. 6(e)-6(f)] footprint patterns generated by the *IPM* [Fig. 6(a)] and the *QIPM* [Fig. 6(b)] *IRP-EMS* in an observation region  $\Psi_{obs}$  of  $75 \times 60$  [m<sup>2</sup>] located in front of the *RP-EMS* are reported.



Despite the relatively small *EMS* aperture and its very limited (binary) reconfiguration capabilities, the *QIPM* configuration [Fig. 6(b)] of the *IRP-EMS* focuses the reflected beam in the desired coverage region  $\Psi_{cov}$  (i.e., along a non-Snell direction) better than the *IPM* one [Fig. 6(a)] with a lower number of sidelobes [Fig. 6(c) vs. Fig. 6(d)]. Moreover, the close fitting between analytically-computed [Figs. 6(c)-6(d)] and *HFSS*-simulated [Figs. 6(e)-6(f)] patterns proves the accuracy of the analytic prediction of the reflection/focusing properties of the *IRP-EMS* layout despite the finite *EMS* aperture and the intrinsic approximations of the analytical model. Such an outcome, which is also in line with the conclusions drawn for the *SP-EMS* case [5][6], further confirms the reliability of the proposed multi-scale design without the need of recurring to expensive full-wave simulations in the on-line synthesis process as well as its effectiveness to control the macro-scale wave manipulation properties of *IRP-EMS*s.

When increasing the *EMS* size  $\Psi_{EMS}$  ( $M = N = 10 \rightarrow M = N = 30$ ) by keeping the same target coverage region  $\Psi_{obs}$  and footprint requirements (18), similar considerations to those of the first numerical experiment hold true. For the sake of completeness and analogously to the  $M \times N = 10 \times 10$  case, Figures 7-9 illustrate the process for configuring the *IRP-EMS* by also comparing the *QIPM*-based approach with the *IPM* one. Figure 7 deals with the current synthesis, while Figure 8 is concerned with the configuration of the *IRP-EMS*, and Figure 9 gives the radiated footprint patterns. More in detail, Figure 7(a) shows the iterative *QIPM/IPM* minimization of the macro-scale cost function (9) to define the reference (phase) current profiles in Figs. 7(b)-7(c) that are approximated [Figs. 7(d)-7(e)] by the *SbD*-optimized setups [Figs. 8(b)-8(c)] of the *IRP-EMS* in Fig. 8(a) to afford the footprint patterns in Figs. 9(a)-9(b). Once again, the constrained nature of the *QIPM* solution [Fig. 7(c)] allows one to better configure [Fig. 8(c)] the single-bit *RP-EMS* [Fig. 8(a)] for more faithfully fulfilling the target coverage [Fig. 9(b)]. The improved focusing performance of the *QIPM*-based control are quantified by the value of the *footprint coverage index*  $\gamma$ ,

$$\gamma \triangleq \frac{W_{cov}}{W_{ext}} \quad (20)$$

where  $W_{\Psi} \triangleq \frac{1}{2\eta_0} \int_{\Psi} F(\tilde{x}, \tilde{y}, \tilde{z}; t) d\tilde{x}d\tilde{y}d\tilde{z}$  is the power reflected in the  $\Psi$  region and  $\Psi_{ext} = \Psi_{obs} - \Psi_{cov}$ , which is equal to  $\gamma^{QIPM} \approx 4.3 \times 10^{-1}$ , while  $\gamma^{IPM} \approx 3.6 \times 10^{-1}$  [Fig. 10(a)].

In order to give the interested readers a more exhaustive picture of the advantages of using the

*QIPM* approach instead of the *IPM* one when dealing with discrete *RP-EMS*s, Figure 10(a) compares the behavior of  $\gamma^{IPM}$  and  $\gamma^{QIPM}$  versus the size of the *IRP-EMS* aperture by reporting the relative index  $\Delta\gamma$  ( $\Delta\gamma \triangleq \frac{\gamma^{QIPM} - \gamma^{IPM}}{\gamma^{IPM}}$ ), as well. As it can be observed, the proposed method (Sect. 3) always determines a configuration of the same *IRP-EMS* that better focuses the reflected power towards the coverage region  $\Psi_{cov}$  (i.e.,  $\gamma^{QIPM} > \gamma^{IPM}$ ) with a non-negligible improvement of the power efficiency [i.e.,  $8\% \leq \Delta\gamma \leq 30\%$  - Fig. 10(a)] also when wide apertures are at hand.

For illustrative purposes, the synthesized ON/OFF configurations of the *IRP-EMS* [Figs. 10(b)-10(e)] and the corresponding footprint patterns (Fig. 11) when  $M \times N = 50 \times 50$  [Figs. 10(b)-10(c) and Figs. 11(a)-11(b)] and  $M \times N = 200 \times 200$  [Figs. 10(d)-10(e) and Figs. 11(c)-11(d)] are reported, as well. Despite the exponentially increasing complexity of the optimization problem at hand (11) owing to the widening of the discrete solution space [i.e.,  $8.4 \times 10^{270}$  ( $M \times N = 30 \times 30$ ),  $3.7 \times 10^{752}$  ( $M \times N = 50 \times 50$ ), and  $1.5 \times 10^{12041}$  ( $M \times N = 200 \times 200$ ) binary configurations,  $\mathcal{S}(t)$ ], the control method in Sect. 3.2 turns out to be very effective in finding the optimal *IRP-EMS* configuration  $\mathcal{S}^{opt}(t)|_{t=T=1}$  whatever the size of  $\Psi_{EMS}$ , thus improving the beam focusing capabilities of the *IRP-EMS* [Fig. 10(a)] by fully exploiting the aperture enlargement [Fig. 6(d) ( $M \times N = 10 \times 10$ ) vs. Fig. 9(b) ( $M \times N = 30 \times 30$ ) vs. Fig. 11(b) ( $M \times N = 50 \times 50$ ) vs. Fig. 11(d) ( $M \times N = 200 \times 200$ )].

The next numerical experiment is concerned with the case of a *Multi-Static Reconfigurability* ( $t \in \{t_1, t_2\}; t = 1, \dots, T$ ) and it deals with the installation of a *IRP-EMS* to alternatively target the wireless coverage of Piazza della Signoria or Piazzale degli Uffizi in Florence (Italy) (i.e., one of the most frequented urban areas in Europe) that consist of a L-shaped wider square,  $\Psi_{cov}^{(1)}$ , and a narrow adjacent site,  $\Psi_{cov}^{(2)}$ , where the entrance to the Uffizi museum is located [Fig. 12(a)]. The *IRP-EMS*, which has been assumed to be placed at  $d = 15$  [m] on the building in Fig. 12(b), is requested to switch between the “Signoria+Uffizi” coverage (i.e.,  $F^{des}(\tilde{x}, \tilde{y}, \tilde{z}; t)|_{t=t_1}$  as in (18) by setting  $\Psi_{cov} = \Psi_{cov}^{(1)}$ ) and the “Uffizi” coverage (i.e.,  $F^{des}(\tilde{x}, \tilde{y}, \tilde{z}; t)|_{t=t_2}$  as in (18) by setting  $\Psi_{cov} = \Psi_{cov}^{(2)}$ ).

The configurations of the ON/OFF states of a  $M \times N = 30 \times 30$  layout (i.e.,  $\Psi_{EMS} \approx 1.3 \times 1.3$  [ $m^2$ ]), which afford the  $T = 2$  footprint patterns in Figs. 13(c)-13(d), are reported in Figs.

13(a)-13(b). As it can be observed, there are few similarities between the two control maps,  $\mathcal{S}^{opt}(t)|_{t=t_1}$  and  $\mathcal{S}^{opt}(t)|_{t=t_2}$ , even though the coverage regions at hand,  $\{\Psi_{cov}^{(c)}, (c = 1, \dots, C; C = 2)\}$ , partially overlap [Fig. 12(a)]. Such a behavior is not unexpected due to both the strong non-linearity of the control problem at hand (11) and the binary nature of the control *DoFs*.

Concerning the distribution of the radiated power pattern, Figure 14 confirms the effectiveness of the synthesized layouts in fulfilling the coverage requirements, the footprint patterns faithfully overlapping the area of interest, despite the irregular geometries of the regions-of-interest and the relatively limited number of reconfigurable states [ $\leq 1$  [Kbit] - Fig. 8(a)]. On the other hand, it is also worth noticing that, although the wireless coverage of the “Signoria+Uffizi” area,  $\Psi_{cov}^{(1)}$ , is a more challenging problem than that of the “Uffizi” site,  $\Psi_{cov}^{(2)}$ , since it requires the *IRP-EMS* focuses the reflected power also at very low elevation angles with respect to its location [Fig. 13(c)], the amount of power reflected by the *IRP-EMS* is kept almost unaltered (i.e.,  $\frac{W_{cov}^{(2)}}{W_{cov}^{(1)}} \approx 0.78$ ).

The ability to afford more elaborated/over-constrained footprints by controlling a single-bit *RP-EMS* has been assessed with the synthesis of a  $M \times N = 100 \times 100$  *IRP-EMS* devoted to manipulate the reflected power for matching the “ELEDIA” logo pattern [Fig. 15(b)]. The plot of the full-wave simulated footprint pattern,  $F^{opt}(\tilde{x}, \tilde{y}, \tilde{z}; t)|_{t=1}$ , in an observation region  $\Psi_{obs}^{(c)}$  of extension  $80 \times 40$  [m<sup>2</sup>] [Fig. 15(b)] proves the reliability of the *EMS* configuration  $\mathcal{S}^{opt}(t)|_{t=T=1}$  in Fig. 15(a) to match the coverage requirements on a complex region  $\Psi_{cov}$ . The readers are suggested to notice that this test case has been already successfully addressed in [5] with *SP-EMSs*, but here the *DoFs* are far less than those available in the *SP-EMS* case [5].

Finally, the numerical assessment ends with a test on the performance of the proposed *IRP-EMS* synthesis method in a scenario that needs a *Dynamic Multi-Beam (C = 3) Reconfigurability*. More in detail, the problem at hand is that of  $C = 3$  users, each occupying a coverage region  $\Psi_{cov}^{(c)}$  ( $c = 1, \dots, C$ ) of size  $10 \times 10$  [m<sup>2</sup>], that move at different speeds in different directions as sketched in Fig. 16. By still considering the  $M \times N = 100 \times 100$  *IRP-EMS* aperture, the plots of the footprint pattern [Figs. 17(e)-17(h)] radiated by the corresponding ON/OFF configuration of the *EMS* [Figs. 17(a)-17(d)] in  $T = 4$  subsequent time-instants confirm that

such a technological solution fits the users' needs without installing multiple *RP-EMS*s or using multi-bit-per-atom reconfiguration schemes.

From a computational perspective and to give some insights on the burden for dynamically managing an *EMS*-driven wireless planning, let us consider that a  $t$ -th ( $t = 1, \dots, T$ ) reconfiguration of the  $M \times N = 100 \times 100$  *IRP-EMS* for the last scenario (Fig. 16) required less than 0.2 [s] to a non-optimized MATLAB implementation of the control algorithm (Sects. 3.1-3.2) running on a standard laptop equipped with a single-core 1.6 GHz CPU. Such a quite impressive result has been obtained thanks to the profitable integration of the *QIPM* strategy (Sect. 3.1) and the *SbD*-based binary optimization (Sect. 3.2). Moreover, to the best of our knowledge on the state-of-the-art literature on *EMS*s, it turns out that the proposed *EMS* implementation/control can be properly considered as a suitable candidate/tool for the real-time coverage of time-varying wireless scenarios.

## 5 Conclusions

An innovative method for the synthesis of *RP-EMS*s, based on single-bit meta-atoms able to support advanced propagation manipulation features in *SEME* scenarios, has been proposed. The arising multi-scale optimization problem has been addressed by means of a two-step approach starting from the design of a meta-atom that features only a single-bit reconfiguration. First, a discrete-phase current, which radiates a field distribution fitting complex user-defined requirements on the footprint pattern, has been computed. Then, a digital *SbD*-based optimization has been carried out to set the binary configuration of the *RP-EMS* atoms that supports such a reference discrete-phase current.

To the best of the authors' knowledge on the state-of-the art literature, the main theoretical and methodological advancements of this work lie in:

- the assessment that *RP-EMS* architectures featuring single-bit meta-atoms can allow complex wave manipulations without the need of continuous phase variations [5][6];
- the derivation of an approach for the control of the *RP-EMS* to afford complex footprint shapes and not only pencil beams [9];

- the non-trivial extension of the synthesis paradigm, adopted so far to synthesize static reflectarrays and *SP-EMSs* [5][6][21], to minimum-complexity *RP-EMSs* by deriving a computationally effective reconfiguration method.

From the numerical validation, the following outcomes can be drawn:

- the *QIPM*-based approach for the definition of the reference currents significantly improves the coverage efficiency with respect to state-of-the-art techniques [5] regardless of the *IRP-EMS* aperture at hand [Fig. 10(a)];
- despite the minimum complexity of the meta-atoms ( $B = 1$ ), the synthesized *RP-EMSs* feature advanced wave manipulation properties in realistic scenarios (Fig. 14) as well as in very complex “demonstrative” cases (e.g., Fig. 15);
- the proposed method turns out to be an enabling tool for multi-beam reconfiguration and/or independent user-tracking through *IRP-EMS* layouts (Fig. 16).

Future works, beyond the scope of this manuscript, will be aimed at assessing the performance of the proposed method when using multi-bit meta-atoms and or different meta-atom geometries.

## Acknowledgements

This work benefited from the networking activities carried out within the Project “Cloaking Metasurfaces for a New Generation of Intelligent Antenna Systems (MANTLES)” (Grant No. 2017BHFZKH) funded by the Italian Ministry of Education, University, and Research under the PRIN2017 Program (CUP: E64I19000560001). Moreover, it benefited from the networking activities carried out within the Project “SPEED” (Grant No. 61721001) funded by National Science Foundation of China under the Chang-Jiang Visiting Professorship Program, the Project ‘Inversion Design Method of Structural Factors of Conformal Load-bearing Antenna Structure based on Desired EM Performance Interval’ (Grant no. 2017HZJXSZ) funded by the National Natural Science Foundation of China, and the Project ‘Research on Uncertainty Factors and

Propagation Mechanism of Conformal Loab-bearing Antenna Structure' (Grant No. 2021JZD-003) funded by the Department of Science and Technology of Shaanxi Province within the Program Natural Science Basic Research Plan in Shaanxi Province. A. Massa wishes to thank E. Vico for her never-ending inspiration, support, guidance, and help.

## Appendix

### Expression of $\overline{E}_{mn}(t)$ and $\overline{H}_{mn}(t)$

The surface averaged fields  $\overline{E}_{mn}(t)$  and  $\overline{H}_{mn}(t)$  can be expressed as [5][6][11]

$$\overline{E}_{mn}(t) = \frac{\int_{-\frac{M\Delta x}{2}}^{\frac{M\Delta x}{2}} \int_{-\frac{N\Delta y}{2}}^{\frac{N\Delta y}{2}} \left\{ \overline{\Gamma} + \overline{\Gamma}_{mn}(t) \right\} \cdot \overline{E}^{inc}(x, y, 0) \Omega_{mn}(x, y) dx dy}{2 \times \Delta x \times \Delta y}, \quad (21)$$

and

$$\overline{H}_{mn}(t) = \frac{\int_{-\frac{M\Delta x}{2}}^{\frac{M\Delta x}{2}} \int_{-\frac{N\Delta y}{2}}^{\frac{N\Delta y}{2}} \left\{ \mathbf{k}^{inc} \times \overline{E}^{inc}(x, y, 0) + \mathbf{k}^{ref} \times \overline{\Gamma}_{mn}(t) \cdot \overline{E}^{inc}(x, y, 0) \right\} \Omega_{mn}(x, y) dx dy}{2 \times \Delta x \times \Delta y \times \eta_0 \times k_0} \quad (22)$$

respectively, where  $\overline{\Gamma}_{mn}(t)$  is the local reflection tensor in the  $(m, n)$ -th cell [5][6][11] [ $\overline{\Gamma}_{mn}(t) = \mathbb{Y}\{\mathbf{g}; s_{mn}(t)\}$ ],  $\overline{E}^{inc}$  is the incident electric field [32]

$$\overline{E}^{inc}(x, y, z) \triangleq (E_{\perp}^{inc} \hat{\mathbf{e}}_{\perp} + E_{\parallel}^{inc} \hat{\mathbf{e}}_{\parallel}) \exp[-j\mathbf{k}^{inc} \cdot (x\hat{\mathbf{x}} + y\hat{\mathbf{y}} + z\hat{\mathbf{z}})], \quad (23)$$

where  $\mathbf{k}^{inc}$  is the incident wave vector ( $\mathbf{k}^{inc} \triangleq -k_0 [\sin(\theta^{inc}) \cos(\varphi^{inc}) \hat{\mathbf{x}} + \sin(\theta^{inc}) \sin(\varphi^{inc}) \hat{\mathbf{y}} + \cos(\theta^{inc}) \hat{\mathbf{z}}]$ ),  $\mathbf{k}^{ref}$  is the corresponding reflected wave vector according to standard plane wave theory [11], and  $\hat{\mathbf{e}}_{\perp} = \frac{\mathbf{k}^{inc} \times \hat{\mathbf{z}}}{|\mathbf{k}^{inc} \times \hat{\mathbf{z}}|}$  and  $\hat{\mathbf{e}}_{\parallel} = \frac{\hat{\mathbf{e}}_{\perp} \times \mathbf{k}^{inc}}{|\hat{\mathbf{e}}_{\perp} \times \mathbf{k}^{inc}|}$  are the ‘‘perpendicular’’ and ‘‘parallel’’ unit vectors (i.e., *TE* and *TM* modes) [5][6][11].

## References

- [1] C. Liaskos, S. Nie, A. Tsioliariidou, A. Pitsillides, S. Ioannidis, and I. Akyildiz, "A new wireless communication paradigm through software-controlled metasurfaces," *IEEE Commun. Mag.*, vol. 56, no. 9, pp. 162-169, 2018.
- [2] M. Di Renzo, M. Debbah, D.-T. Phan-Huy, A. Zappone, M.-S. Alouini, C. Yuen, V. Sciancalepore, G. C. Alexandropoulos, J. Hoydis, H. Gacanin, J. De Rosny, A. Bounceur, G. Lerosey, and M. Fink, "Smart radio environments empowered by reconfigurable AI metasurfaces: An idea whose time has come," *EURASIP J. Wireless Commun. Netw.*, vol. 129, pp. 1-20, 2019.
- [3] M. Di Renzo, A. Zappone, M. Debbah, M.-S. Alouini, C. Yuen, J. De Rosny, and S. Tretyakov, "Smart radio environments empowered by reconfigurable intelligent surfaces: How it works, state of research, and the road ahead," *IEEE J. Sel. Areas Comm.*, vol. 38, no. 11, pp. 2450-2525, Nov. 2020.
- [4] A. Massa, A. Benoni, P. Da Ru, S. K. Goudos, B. Li, G. Oliveri, A. Polo, P. Rocca, and M. Salucci, "Designing smart electromagnetic environments for next-generation wireless communications," *Telecom*, vol. 2, no. 2, pp. 213-221, 2021.
- [5] G. Oliveri, P. Rocca, M. Salucci, and A. Massa, "Holographic smart EM skins for advanced beam power shaping in next generation wireless environments," *IEEE J. Multiscale Multiphysics Computat. Techn.*, vol. 6, pp. 171-182, Oct. 2021.
- [6] G. Oliveri, F. Zardi, P. Rocca, M. Salucci, and A. Massa, "Building a smart EM environment - AI-Enhanced aperiodic micro-scale design of passive EM skins," *IEEE Trans. Antennas Propag.*, to be published.
- [7] W. Tang, J. Dai, M. Chen, X. Li, Q. Cheng, S. Jin, K. Wong, and T. J. Cui, "Subject editor spotlight on programmable metasurfaces: The future of wireless," *IET Electron. Lett.*, vol. 55, no. 7, pp. 360-361, 2019.

- [8] M. Di Renzo, K. Ntontin, J. Song, F. H. Danufane, X. Qian, F. Lazarakis, J. De Rosny, D.-T. Phan-Huy, O. Simeone, R. Zhang, M. Debbah, G. Lerosey, M. Fink, S. Tretyakov, and S. Shamai, "Reconfigurable intelligent surfaces vs. relaying: Differences, similarities, and performance comparison," *IEEE Open J. Comm. Soc.*, vol. 1, pp. 798-807, 2020.
- [9] J. C. Liang, Q. Cheng, Y. Gao, C. Xiao, S. Gao, L. Zhang, S. Jin, and T. J. Cui, "An angle-insensitive 3-Bit reconfigurable intelligent surface," *IEEE Trans. Antennas Propag.*, to be published, doi: 10.1109/TAP.2021.3130108.
- [10] P. Callaghan, P. Giannakou, S. G. King, M. Shkunov, and P. R. Young, "Linearly polarized reconfigurable reflectarray surface," *IEEE Trans. Antennas Propag.*, vol. 69, no. 10, pp. 6480-6488, Oct. 2021.
- [11] F. Yang and Y. Rahmat-Samii, *Surface Electromagnetics with Applications in Antenna, Microwave, and Optical Engineering*, Cambridge, UK: Cambridge University Press, 2019.
- [12] P. Rocca, P. Da Ru, N. Anselmi, M. Salucci, G. Oliveri, D. Erricolo, and A. Massa, "On the design of modular reflecting EM skins for enhanced urban wireless coverage," *IEEE Trans. Antennas Propag.*, to be published, doi: 10.1109/TAP.2022.3146870.
- [13] A. Benoni, M. Salucci, G. Oliveri, P. Rocca, B. Li, and A. Massa, "Planning of EM skins for improved quality-of-service in urban areas," *IEEE Trans. Antennas Propag.*, under review.
- [14] J. A. Hodge, K. V. Mishra, and A. I. Zaghloul, "Intelligent time-varying metasurface transceiver for index modulation in 6G wireless networks," *IEEE Antennas Wireless Propag. Lett.*, vol. 19, no. 11, pp. 1891-1895, Nov. 2020.
- [15] A. Massa and M. Salucci, "On the design of complex EM devices and systems through the system-by-design paradigm - A framework for dealing with the computational complexity," *IEEE Trans. Antennas Propag.*, vol. 70, no. 2, pp. 1328-1343, Feb. 2022.



- [16] S. Gong, X. Lu, D. T. Hoang, D. Niyato, L. Shu, D. I. Kim, and Y.-C. Liang, "Toward smart wireless communications via intelligent reflecting surfaces: A contemporary survey," *IEEE Communications Surveys & Tutorials*, vol. 22, no. 4, pp. 2283-2314, 2020.
- [17] A. Pitilakis, O. Tsilipakos, F. Liu, K. M. Kossifos, A. C. Tasolamprou, D.-H. Kwon, M. S. Mirmoosa, D. Manassis, N. V. Kantartzis, C. Liaskos, M. A. Antoniadis, J. Georgiou, C. M. Soukoulis, M. Kafesaki, and S. A. Tretyakov, "A multi-functional reconfigurable metasurface: Electromagnetic design accounting for fabrication aspects," *IEEE Trans. Antennas Propag.*, vol. 69, no. 3, pp. 1440-1454, Mar. 2021.
- [18] L. Dai, B. Wang, M. Wang, X. Yang, J. Tan, S. Bi, S. Xu, F. Yang, Z. Chen, M. Di Renzo, C.-B. Chae, and L. Hanzo, "Reconfigurable intelligent surface-based wireless communications: Antenna design, prototyping, and experimental results," *IEEE Access*, vol. 8, pp. 45913-45923, 2020.
- [19] B. G. Kashyap, P. C. Theofanopoulos, Y. Cui, and G. C. Trichopoulos, "Mitigating quantization lobes in mmWave low-bit reconfigurable reflective surfaces," *IEEE Open J. Antennas Propag.*, vol. 1, pp. 604-614, 2020.
- [20] C. Ross, G. Gradoni, Q. J. Lim, and Z. Peng, "Engineering reflective metasurfaces with Ising Hamiltonian and quantum annealing," *IEEE Trans. Antennas Propag.*, in press. doi:10.1109/TAP.2021.3137424
- [21] M. Salucci, A. Gelmini, G. Oliveri, N. Anselmi, and A. Massa, "Synthesis of shaped beam reflectarrays with constrained geometry by exploiting non-radiating surface currents," *IEEE Trans. Antennas Propag.*, vol. 66, no. 11, pp. 5805-5817, Nov. 2018.
- [22] G. Oliveri, F. Viani, N. Anselmi, and A. Massa, "Synthesis of multi-layer WAIM coatings for planar phased arrays within the system-by-design framework," *IEEE Trans. Antennas Propag.*, vol. 63, no. 6, pp. 2482-2496, Jun. 2015.
- [23] G. Oliveri, M. Salucci, N. Anselmi, and A. Massa, "Multiscale System-by-Design synthesis of printed WAIMs for waveguide array enhancement," *IEEE J. Multiscale Multiphysics Computat. Techn.*, vol. 2, pp. 84-96, 2017.

- [24] G. Oliveri, A. Gelmini, A. Polo, N. Anselmi, and A. Massa, "System-by-design multi-scale synthesis of task-oriented reflectarrays," *IEEE Trans. Antennas Propag.*, vol. 68, no. 4, pp. 2867-2882, Apr. 2020.
- [25] G. Oliveri, A. Polo, M. Salucci, G. Gottardi, and A. Massa, "SbD-based synthesis of low-profile WAIM superstrates for printed patch arrays," *IEEE Trans. Antennas Propag.*, vol. 69, no. 7, pp. 3849-3862, Jul. 2021.
- [26] M. A. Ricoy and J. L. Volakis, "Derivation of generalized transition/boundary conditions for planar multiple-layer structures," *Radio Sci.*, vol. 25, pp. 391-405, 1990.
- [27] K. Achouri, M. A. Salem, and C. Caloz, "General metasurface synthesis based on susceptibility tensors," *IEEE Trans. Antennas Propag.*, vol. 63, no. 7, pp. 2977-2991, Jul. 2015.
- [28] J. A. Encinar and J. A. Zornoza, "Three-layer printed reflectarrays for contoured beam space applications," *IEEE Trans. Antennas Propag.*, vol. 52, no. 5, pp. 1138-1148, May 2004.
- [29] D. R. Prado, M. Arrebola, M. R. Pino, and F. Las-Heras, "Complex reflection coefficient synthesis applied to dual-polarized reflectarrays with cross-polar requirements," *IEEE Trans. Antennas Propag.*, vol. 63, no. 9, pp. 3897-3907, Sep. 2015.
- [30] P. Nayeri, F. Yang, and A. Z. Elsherbeni, "Design of single-feed reflectarray antennas with asymmetric multiple beams using the particle swarm optimization method," *IEEE Trans. Antennas Propag.*, vol. 61, no. 9, pp. 4598-4605, Sep. 2013.
- [31] D. M. Pozar, S. D. Targonski, and R. Pokuls, "A shaped-beam microstrip patch reflectarray," *IEEE Trans. Antennas Propag.*, vol. 47, no. 7, pp. 1167-1173, Jul. 1999.
- [32] A. Osipov and S. Tretyakov, *Modern electromagnetic scattering theory with applications*. John Wiley & Sons, 2017.
- [33] M. Salucci, L. Tenuti, G. Oliveri, and A. Massa, "Efficient prediction of the EM response of reflectarray antenna elements by an advanced statistical learning method," *IEEE Trans. Antennas Propag.*, vol. 66, no. 8, pp. 3995-4007, Aug. 2018.

- [34] P. Rocca, M. Benedetti, M. Donelli, D. Franceschini, and A. Massa, “Evolutionary optimization as applied to inverse problems,” *Inverse Problems*, vol. 25, pp. 1-41, Dec. 2009.
- [35] ANSYS Electromagnetics Suite - HFSS (2021). ANSYS, Inc.
- [36] H. Yang, F. Yang, X. Cao, S. Xu, J. Gao, X. Chen, M. Li, and T. Li, “A 1600-element dual-frequency electronically reconfigurable reflectarray at X/Ku-band,” *IEEE Trans. Antennas Propag.*, vol. 65, no. 6, pp. 3024-3032, Jun. 2017.
- [37] M. Ciydem and E. A. Miran, “Dual-polarization wideband sub-6 GHz suspended patch antenna for 5G base station,” *IEEE Antennas Wireless Propag. Lett.*, vol. 19, no. 7, pp. 1142-1146, Jul. 2020.
- [38] G. Oliveri, D. H. Werner, and A. Massa, “Reconfigurable electromagnetics through metamaterials - A review,” *Proc. IEEE*, vol. 103, no. 7, pp. 1034-1056, Jul. 2015.

## FIGURE CAPTIONS

- **Figure 1.** *Problem geometry.* Sketch of the smart *EM* environment scenario.
- **Figure 2.** *IRP-EMS Design* - Unit cell geometry: (a) top view and 3D CAD model of (b) the meta-atom and zoom on (c) the switching device.
- **Figure 3.** *IRP-EMS Design* - Plots of (a) the phase and (b) the magnitude of the TE/TM components of the local reflection tensor  $\overline{\overline{\Gamma}}_{mn}$  versus the frequency in correspondence with the “ON” ( $s_{mn} = 1$ ) and the “OFF” ( $s_{mn} = 0$ ) states.
- **Figure 4.** *IRP-EMS Control* (“Square” Footprint,  $M = N = 10$ ,  $d = 5$  [m];  $P = 10^2$ ) - Behaviour of (a) the macro-scale cost  $\Phi^{(p)}$  versus the iteration index ( $p = 1, \dots, P$ ) and plot of (b)(c) the phase of the reference current,  $\{\overline{J}^{opt}(x_m, y_n; t); (m = 1, \dots, M; n = 1, \dots, N)\}$ , synthesized with (b) the *IPM*,  $\overline{J}_{IPM}^{opt}$ , and (c) the *QIPM*,  $\overline{J}_{QIPM}^{opt}$ .
- **Figure 5.** *IRP-EMS Control* (“Square” Footprint,  $M = N = 10$ ,  $d = 5$  [m]) - Plots of (a) the distribution of the local error  $\sigma_\ell$  [ $\ell = n + N \times (m - 1); (m = 1, \dots, M; n = 1, \dots, N)$ ]

and of (c)(d) the phase of the current,  $\{\bar{J}^*(x_m, y_n; t); (m = 1, \dots, M; n = 1, \dots, N)\}$ , generated by the *IRP-EMS* (b) configured with (c) the *IPM*-based approach,  $\bar{J}_{IPM}^*$ , or (d) the *QIPM* one,  $\bar{J}_{QIPM}^*$ .

- **Figure 6.** *IRP-EMS Control* (“Square” Footprint,  $M = N = 10$ ,  $d = 5$  [m]) - Plots of (a)(b) the ON/OFF states and the corresponding (c)(d) analytically-computed and (e)(f) HFSS-simulated footprint patterns of (a) the *IPM* and (b) the *QIPM IRP-EMS*.
- **Figure 7.** *IRP-EMS Control* (“Square” Footprint,  $M = N = 30$ ,  $P = 10^2$ ) - Behaviour of (a) the macro-scale cost  $\Phi^{(p)}$  versus the iteration index ( $p = 1, \dots, P$ ) and plots of the phase of (b)(c) the reference current,  $\{\bar{J}^{opt}(x_m, y_n; t); (m = 1, \dots, M; n = 1, \dots, N)\}$ , and of (d)(e) the current,  $\{\bar{J}^*(x_m, y_n; t); (m = 1, \dots, M; n = 1, \dots, N)\}$ , generated by the configured *IRP-EMS* in [Fig. 8(a)] when applying (b)(d) the *IPM*-based approach or (c)(e) the *QIPM* one.
- **Figure 8.** *IRP-EMS Control* (“Square” Footprint,  $M = N = 30$ ,  $d = 5$  [m]) - Plot of (a) the 3D model of the *RP-EMS* and map of (b)(c) the ON/OFF states of the *IRP-EMS* yielded with (b) the *IPM*,  $S_{IPM}^{opt}$ , and (d) the *QIPM*,  $S_{QIPM}^{opt}$ , approaches.
- **Figure 9.** *IRP-EMS Control* (“Square” Footprint,  $M = N = 30$ ,  $d = 5$  [m]) - Plots of the HFSS-simulated footprint pattern radiated by (a) the *IPM* and (b) the *QIPM IRP-EMS*.
- **Figure 10.** *IRP-EMS Control* (“Square” Footprint,  $d = 5$  [m]) - Behaviours of (a) the total,  $\gamma$ , and the relative,  $\Delta\gamma$ , coverage indexes versus the *IRP-EMS* size and maps of (b)-(e) the ON/OFF configurations of the *IRP-EMS* synthesized with (b)(d) the *IPM* and (c)(e) the *QIPM* when (b)(c)  $M \times N = 50 \times 50$  and (d)(e)  $M \times N = 200 \times 200$ .
- **Figure 11.** *IRP-EMS Control* (“Square” Footprint,  $d = 5$  [m]) - Plots of the HFSS-simulated footprint pattern radiated by (a)(c) the *IPM* and (b)(d) the *QIPM IRP-EMS* when (a)(b)  $M \times N = 50 \times 50$  and (c)(d)  $M \times N = 200 \times 200$ .
- **Figure 12.** *IRP-EMS Control* (“Signoria+Uffizi” and “Uffizi” Footprints,  $M = N = 30$ ,  $d = 15$  [m]) - View of (a) the scenario and of (b) the location of the *IRP-EMS*.

- **Figure 13.** *IRP-EMS Control (“Signoria+Uffizi” and “Uffizi” Footprints,  $M = N = 30$ ,  $d = 15$  [m]; QIPM)* - Plots of (a)(b) the ON/OFF states of the *IRP-EMS* and (c)(d) the corresponding HFSS-simulated footprint patterns when focusing on (a)(c) the “Signoria+Uffizi” area and (b)(d) the “Uffizi” area.
- **Figure 14.** *IRP-EMS Control (“Signoria+Uffizi” and “Uffizi” Footprints,  $M = N = 30$ ,  $d = 15$  [m]; QIPM)* - Coverage check when dealing with (a) the “Signoria+Uffizi” and (b) the “Uffizi” coverage scenarios.
- **Figure 15.** *IRP-EMS Control (“ELEDIA” Footprint,  $M = N = 100$ ,  $d = 15$  [m]; QIPM)* - Plots of (a) the ON/OFF states of the *IRP-EMS* and (b) the corresponding HFSS-simulated footprint pattern.
- **Figure 16.** *IRP-EMS Control (Multi-Beam Footprint,  $M = N = 100$ ,  $d = 5$  [m]; QIPM)* - Users’ trajectories.
- **Figure 17.** *IRP-EMS Control (Multi-Beam Footprint,  $M = N = 100$ ,  $d = 5$  [m]; QIPM)* - Plots of (a)-(d) the ON/OFF states of the *IRP-EMS* and (e)-(h) the corresponding HFSS-simulated footprint patterns radiated at (a)(e)  $t = 1$ , (b)(f)  $t = 2$ , (c)(g)  $t = 3$ , and (d)(h)  $t = T$  ( $T = 4$ ).

## TABLE CAPTIONS

- **Table 1.** *IRP-EMS Design* - Geometrical descriptors.

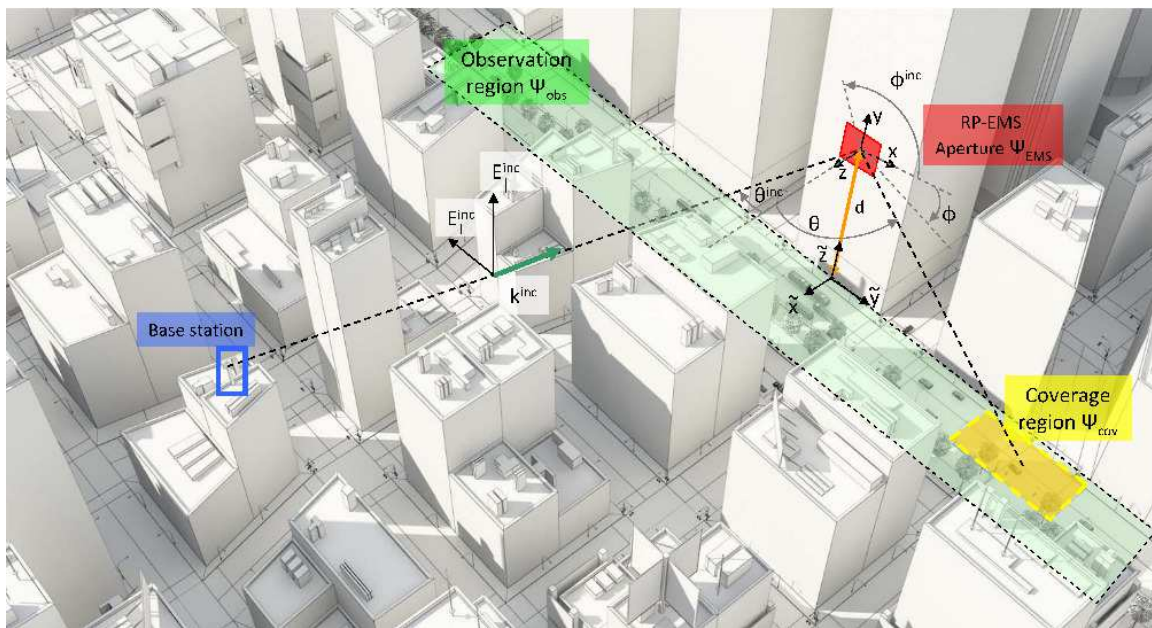
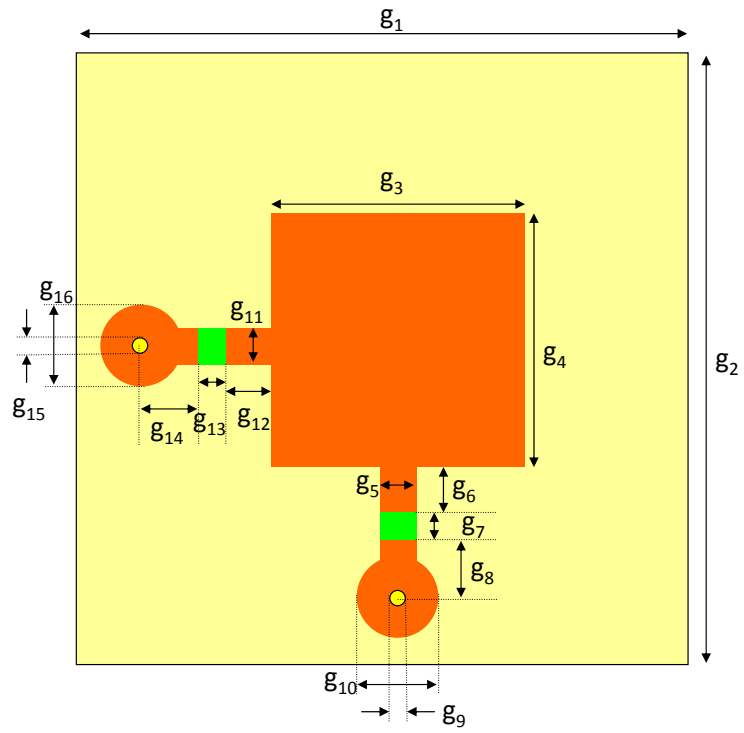
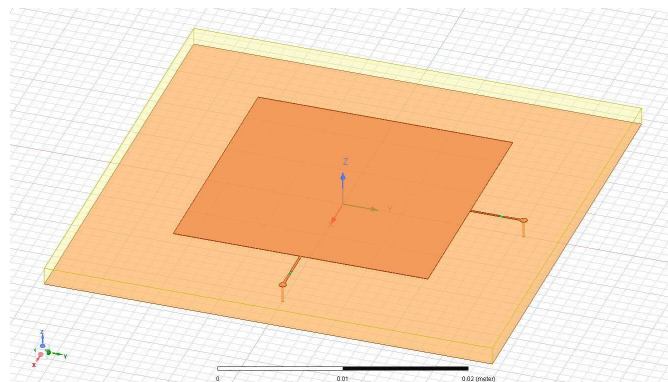


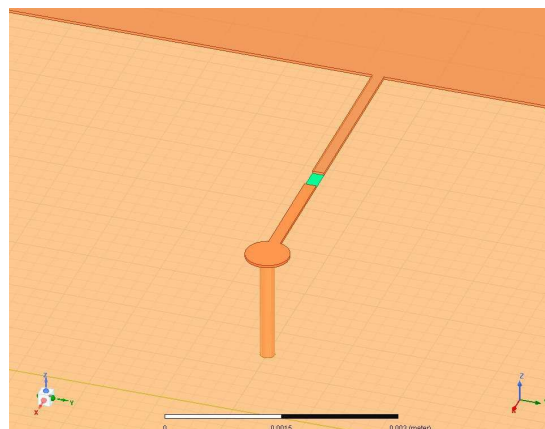
Fig. 1 - G. Oliveri et al., “Multi-Scale Single-Bit *RP-EMS* Synthesis for ...”



(a)

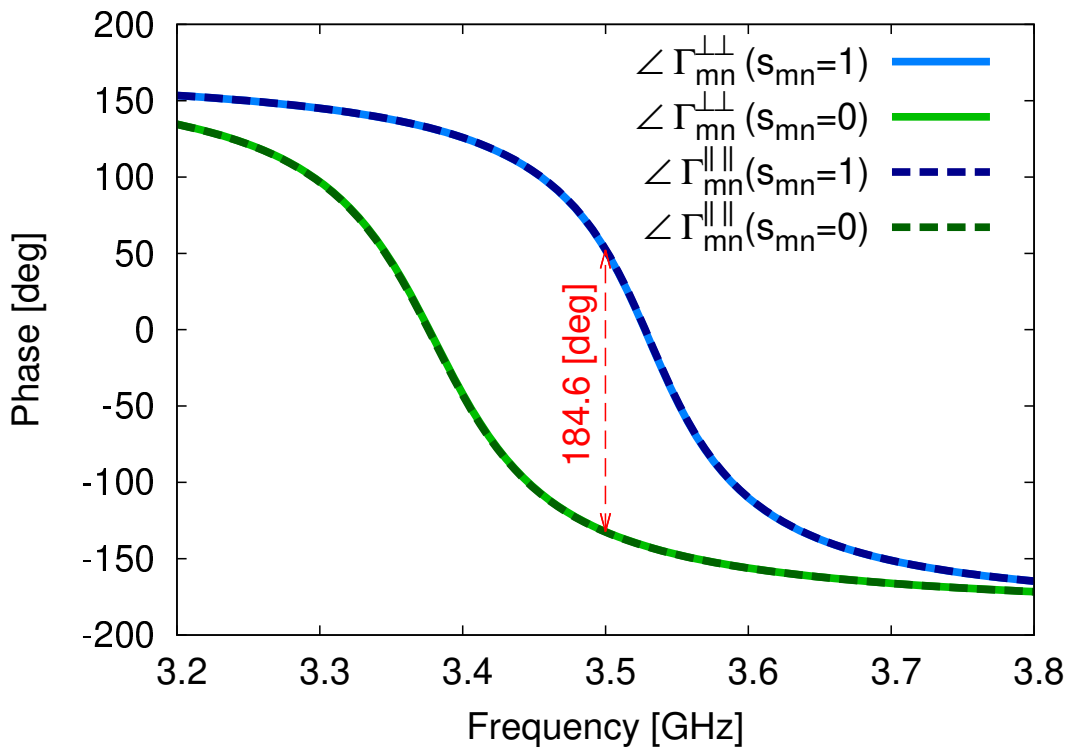


(b)

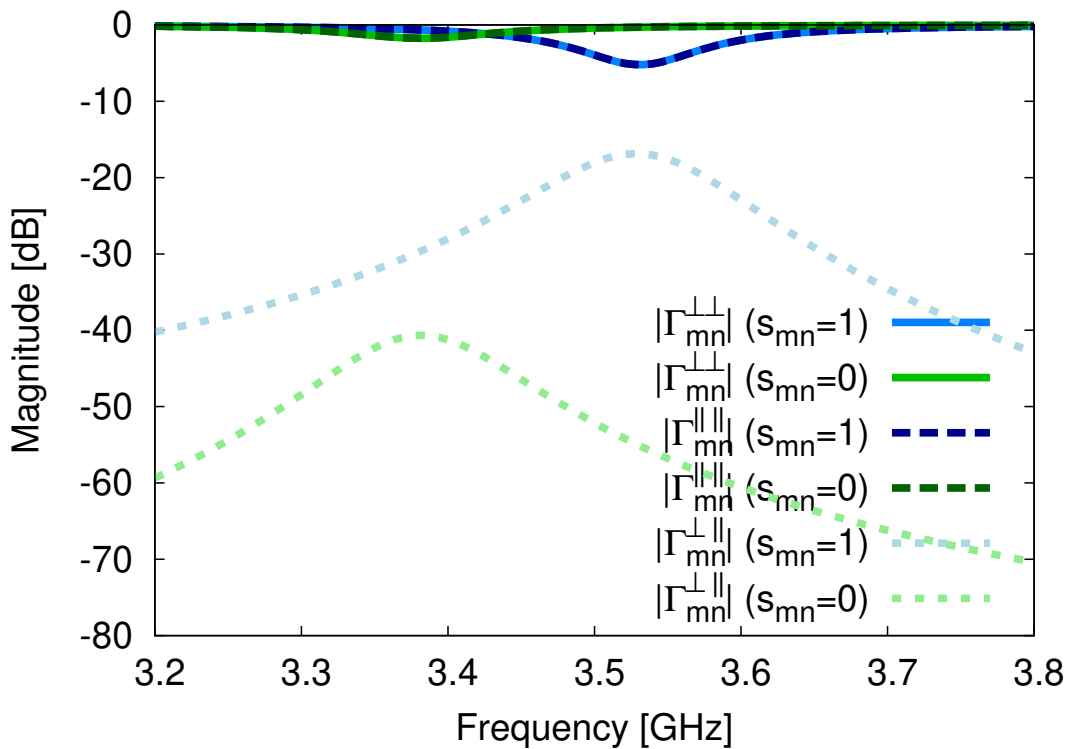


(c)

Fig. 2 - G. Oliveri et al., "Multi-Scale Single-Bit RP-EMS Synthesis for ..."



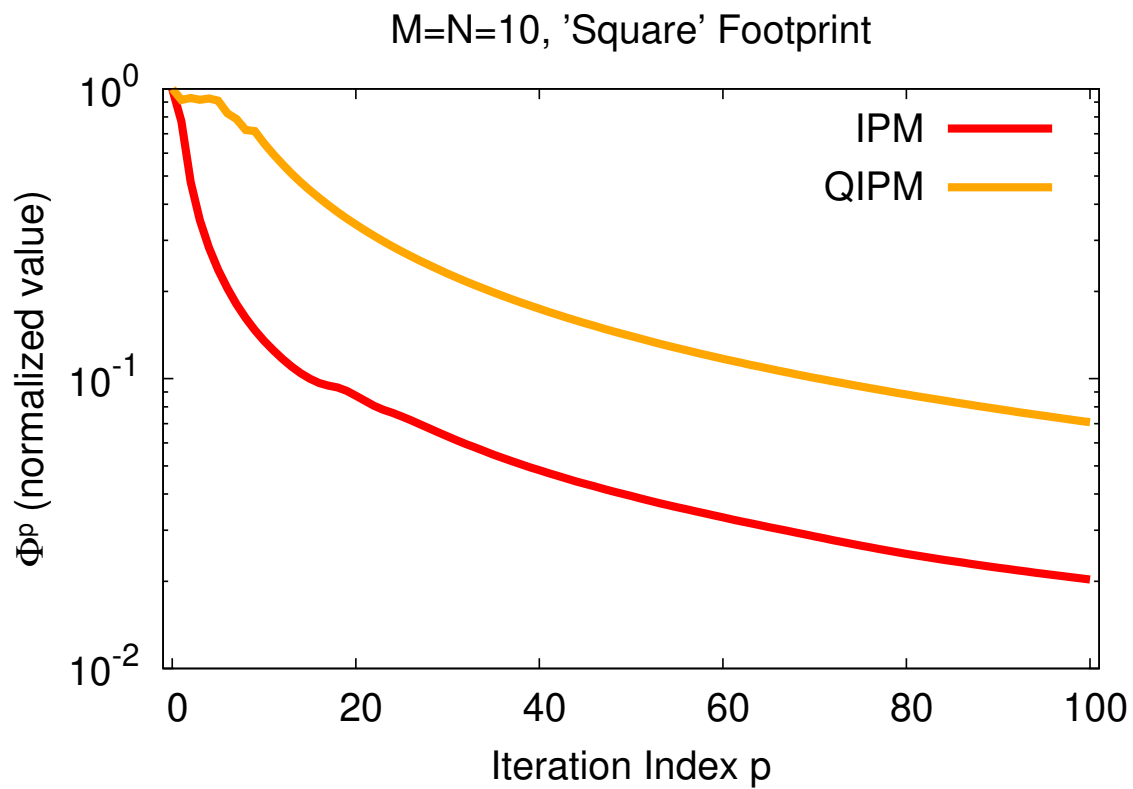
(a)



(b)

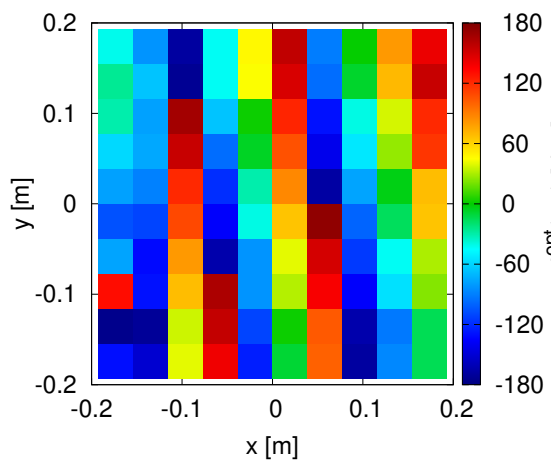
Fig. 3 - G. Oliveri et al., "Multi-Scale Single-Bit RP-EMS Synthesis for ..."





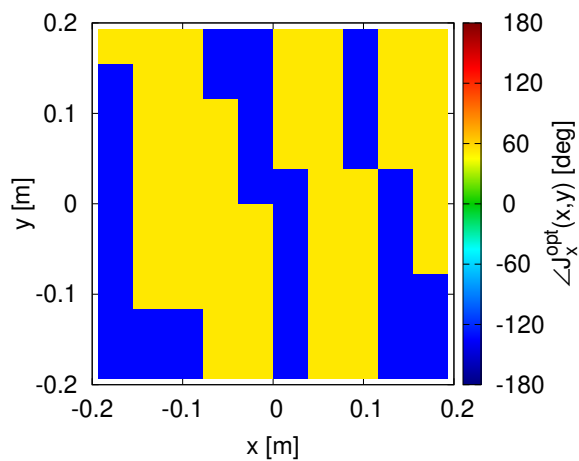
(a)

M=N=10, Footprint 'Square', IPM



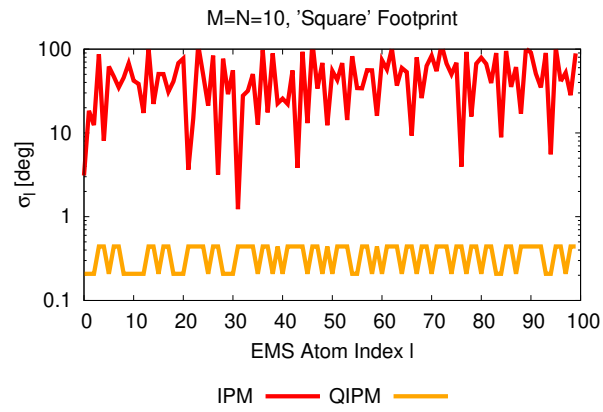
(b)

M=N=10, Footprint 'Square', QIPM

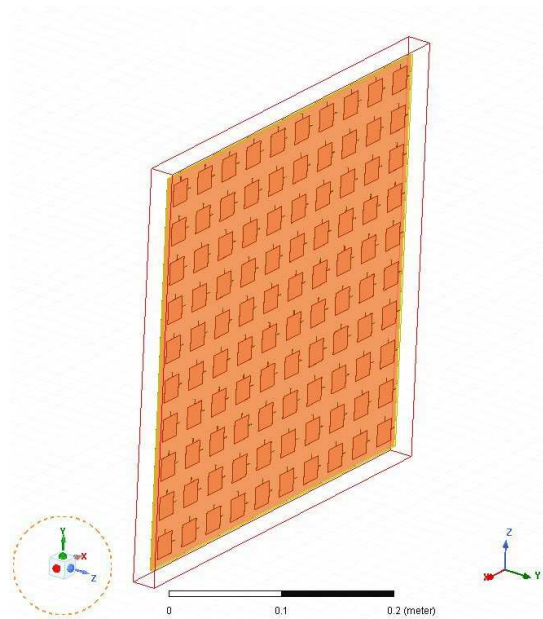


(c)

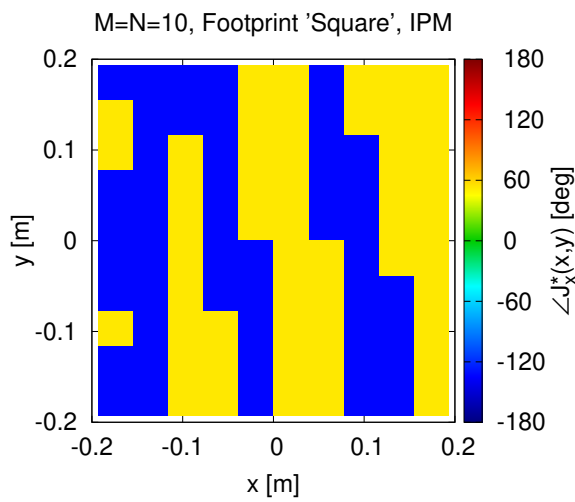
**Fig. 4 - G. Oliveri et al., “Multi-Scale Single-Bit *RP-EMS* Synthesis for ...”**



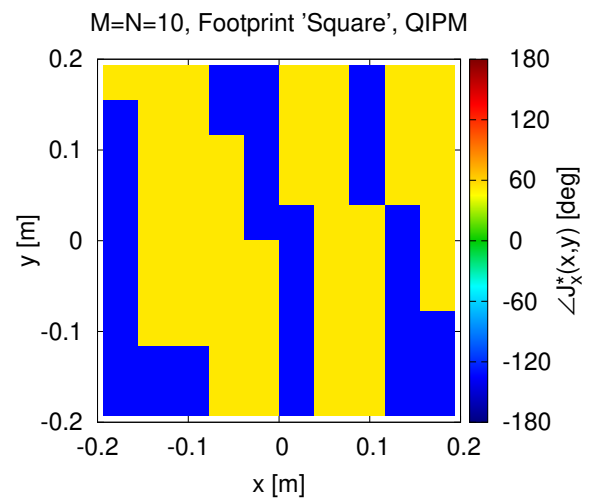
(a)



(b)



(c)



(d)

**Fig. 5 - G. Oliveri et al., “Multi-Scale Single-Bit *RP*-EMS Synthesis for ...”**

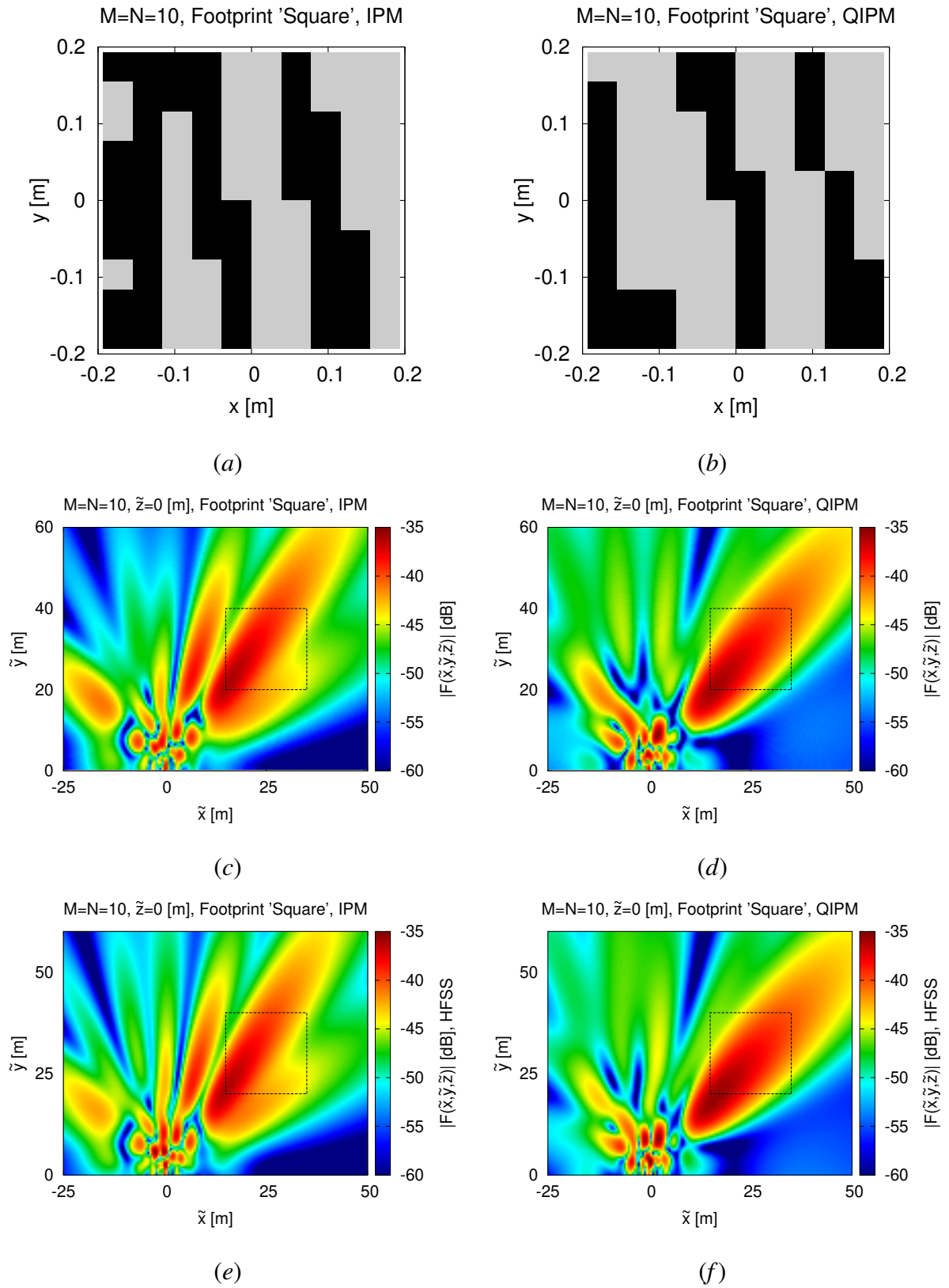
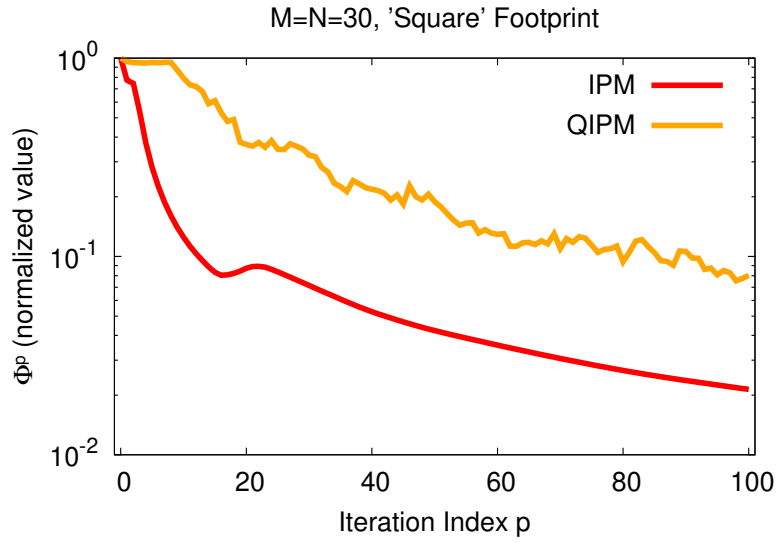
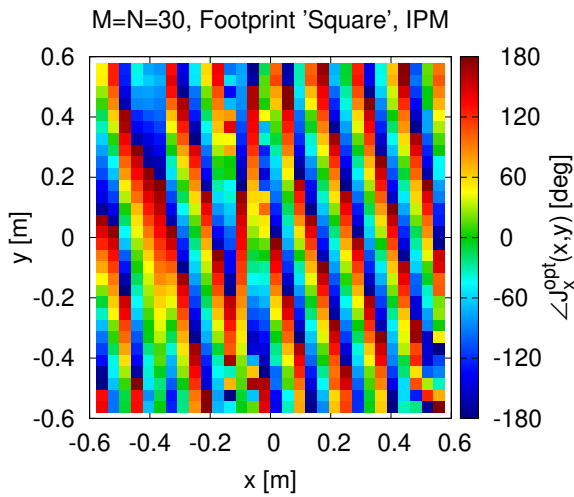


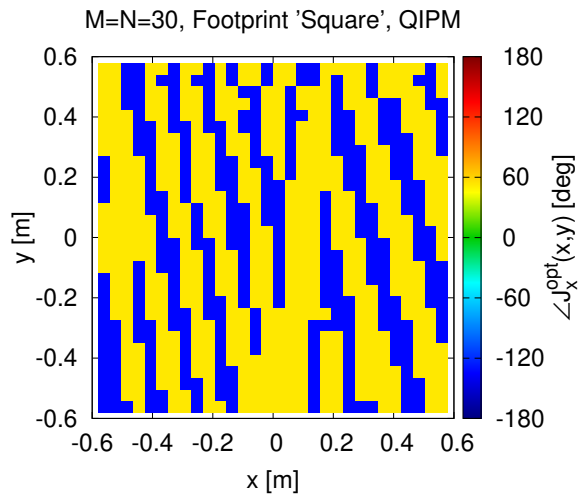
**Fig. 6 - G. Oliveri et al., "Multi-Scale Single-Bit *RP-EMS* Synthesis for ..."**



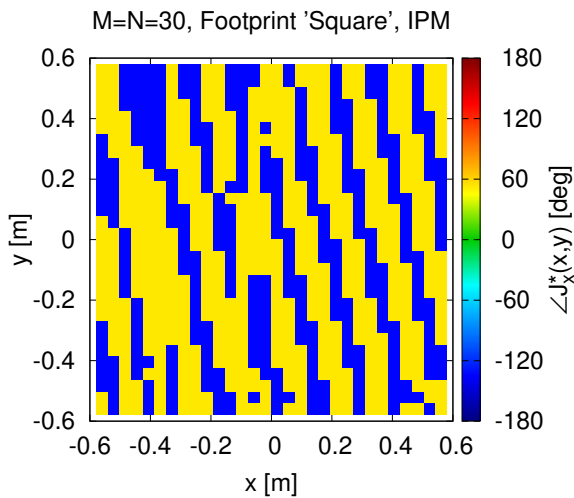
(a)



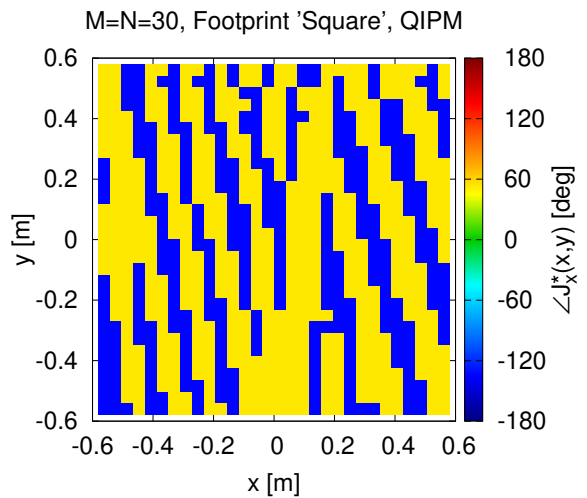
(b)



(c)

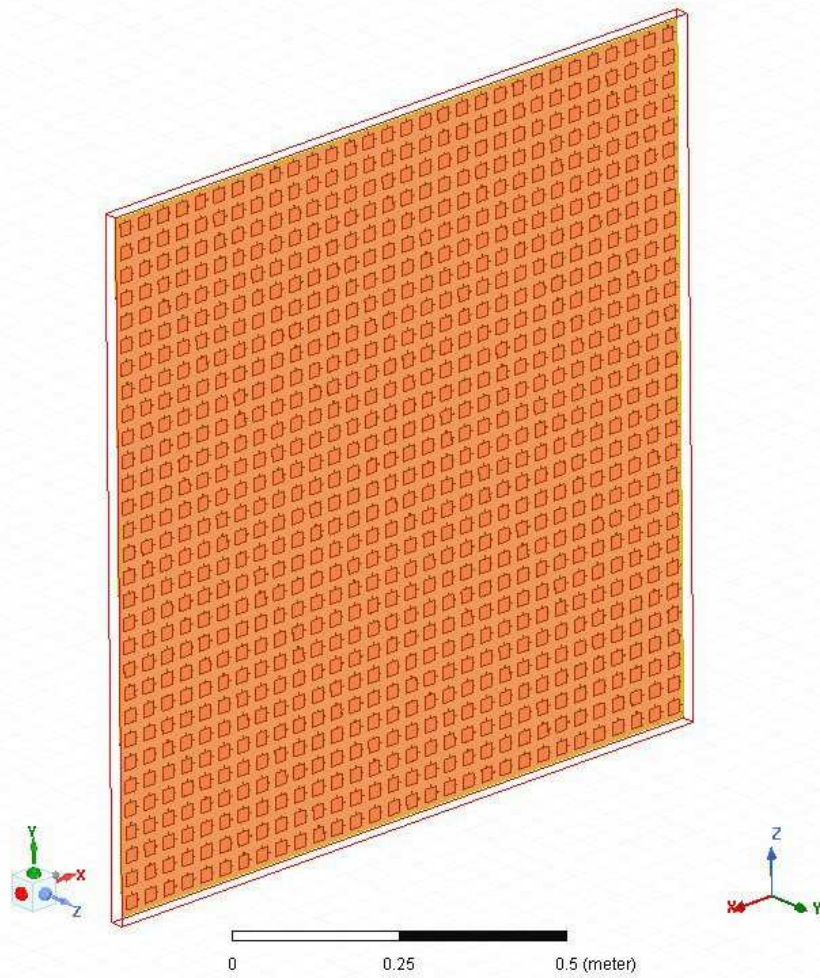


(d)

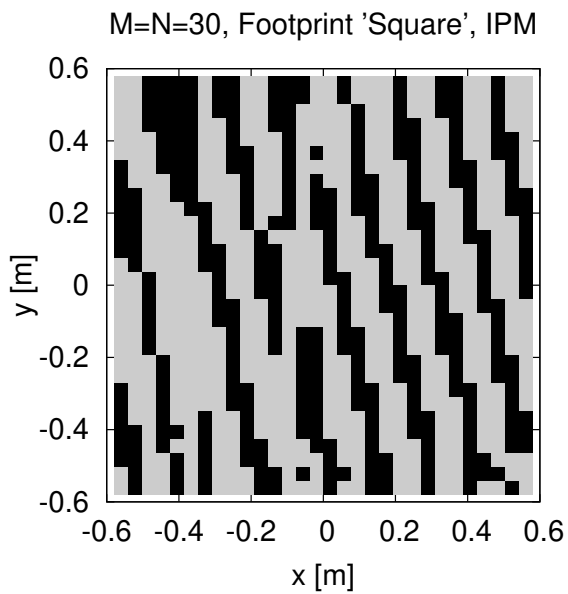


(e)

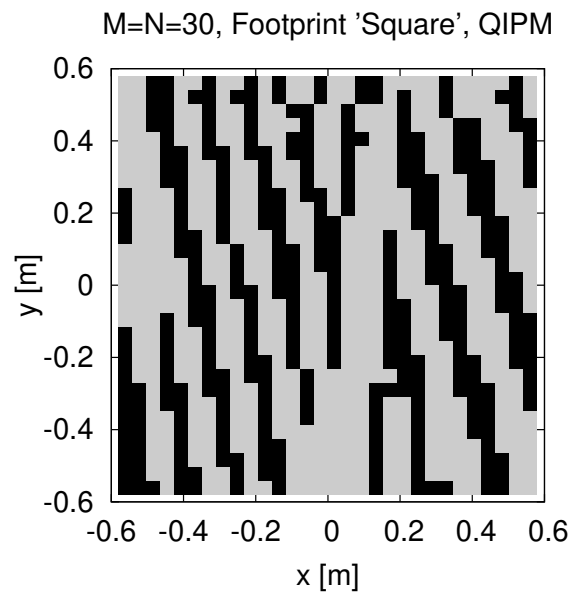
**Fig. 7 - G. Oliveri et al., “Multi-Scale Single-Bit *RP-EMS* Synthesis for ...”**



(a)

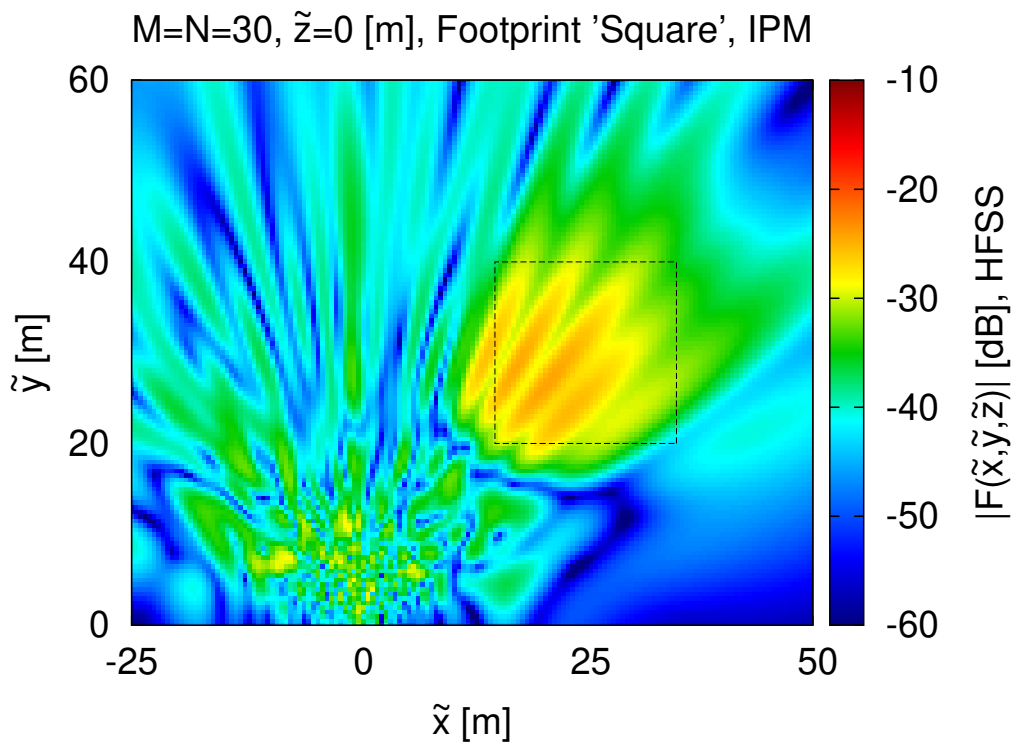


(b)

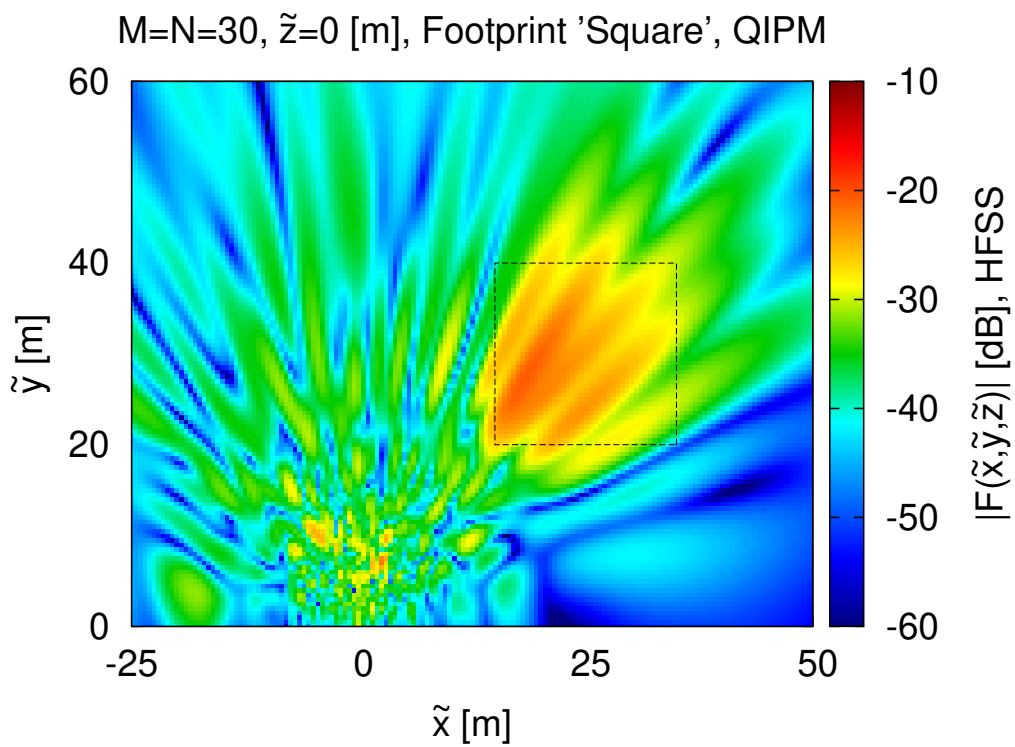


(c)

**Fig. 8 - G. Oliveri et al., “Multi-Scale Single-Bit *RP-EMS* Synthesis for ...”**

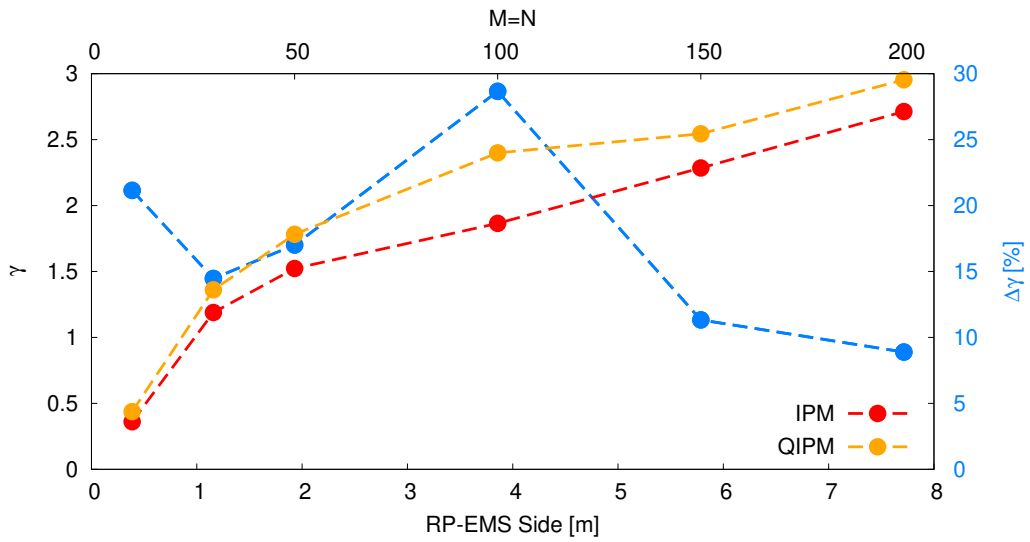


(a)

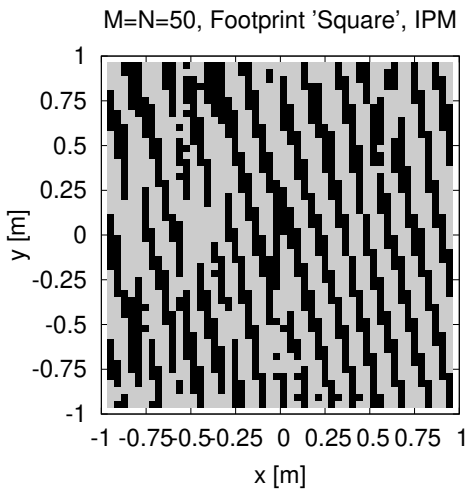


(b)

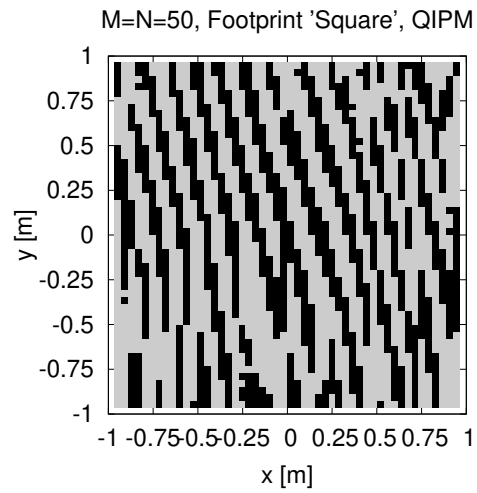
Fig. 9 - G. Oliveri et al., "Multi-Scale Single-Bit *RP-EMS* Synthesis for ..."



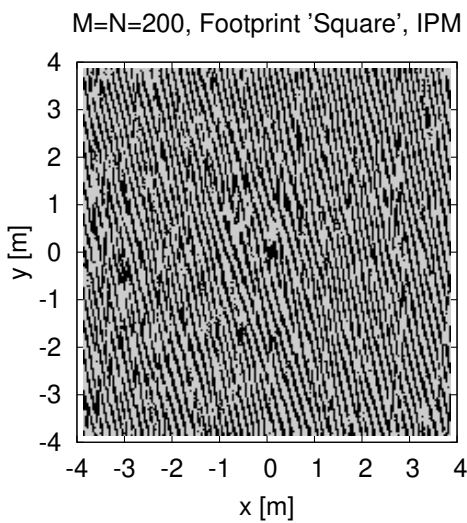
(a)



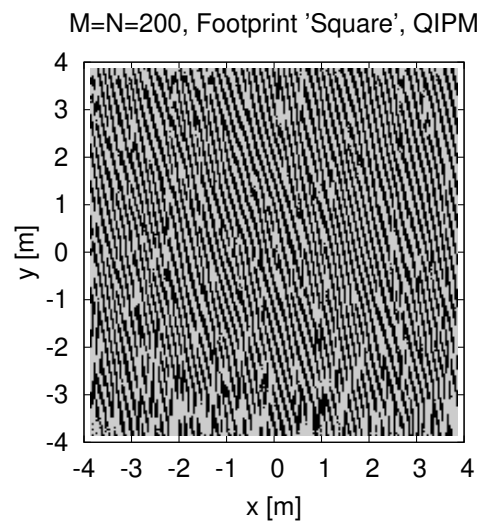
(b)



(c)



(d)



(e)

Fig. 10 - G. Oliveri et al., "Multi-Scale Single-Bit *RP-EMS* Synthesis for ..."

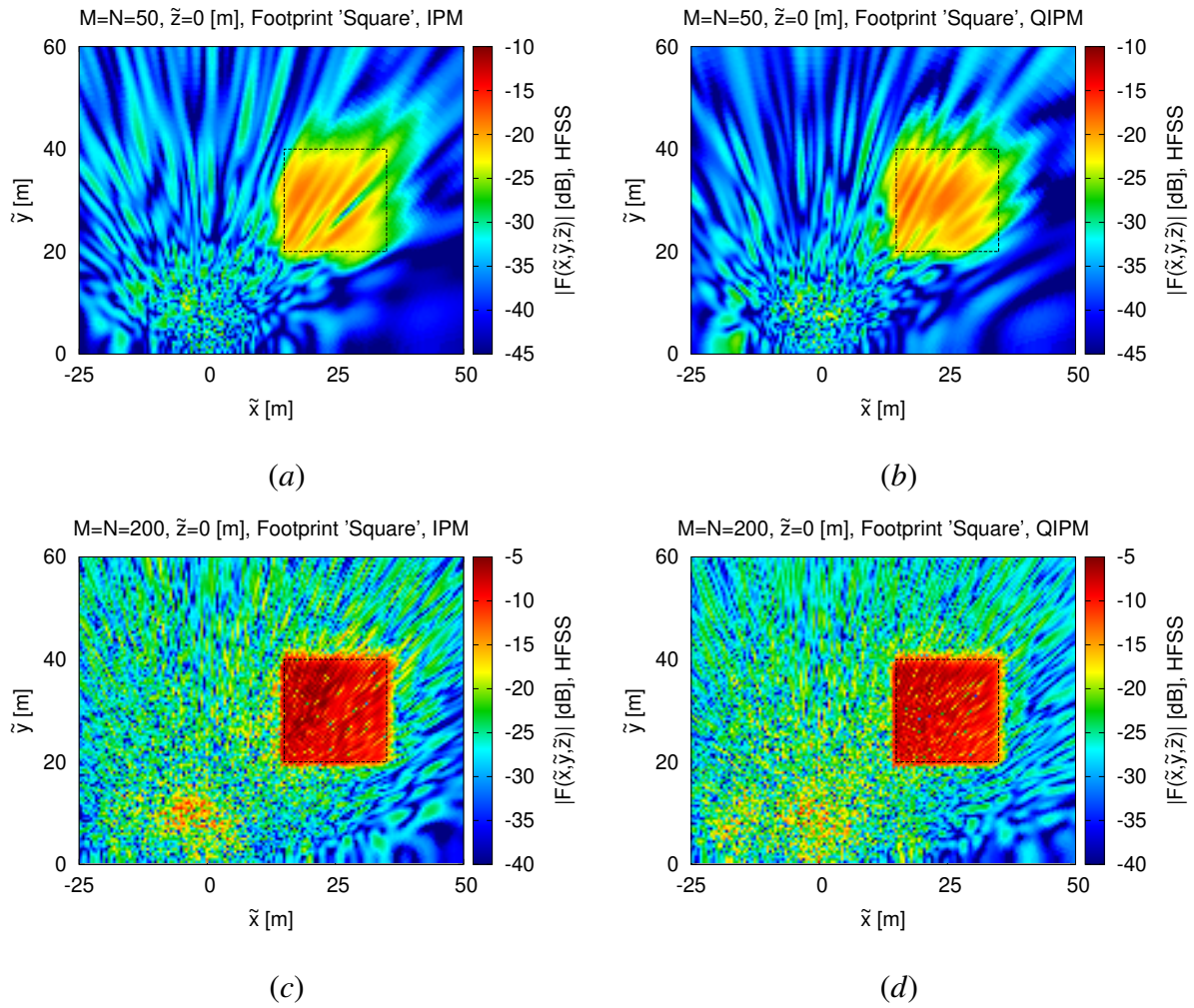


Fig. 11 - G. Oliveri et al., "Multi-Scale Single-Bit *RP-EMS* Synthesis for ..."



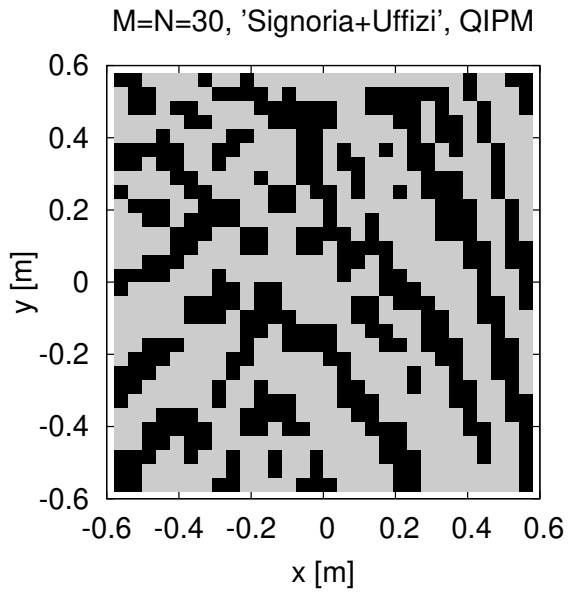


(a)

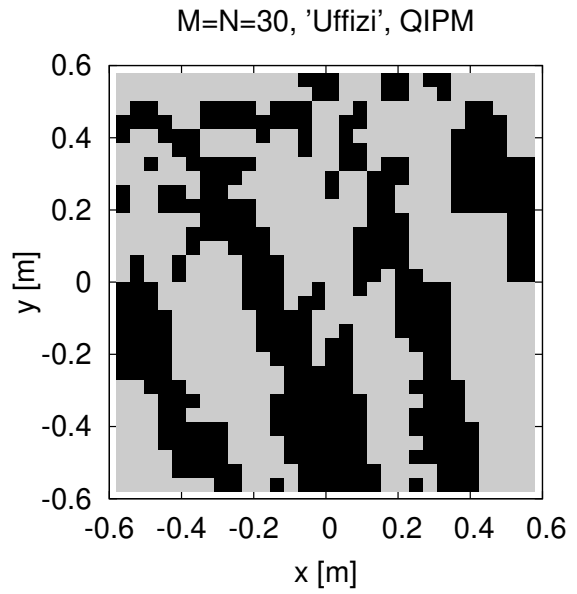


(b)

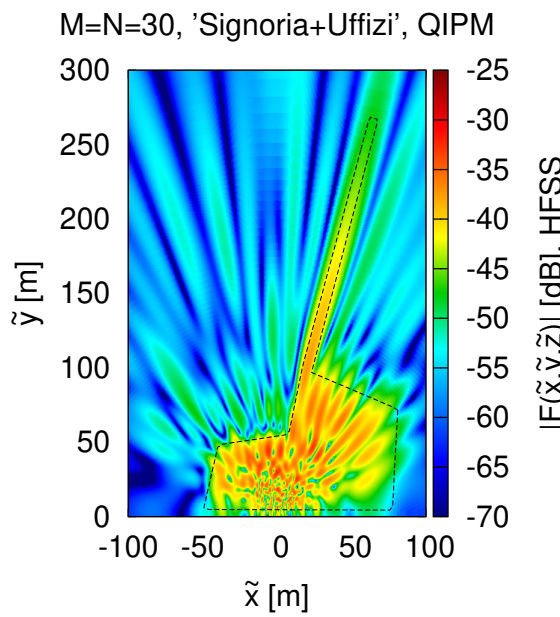
Fig. 12 - G. Oliveri et al., "Multi-Scale Single-Bit *RP-EMS* Synthesis for ..."



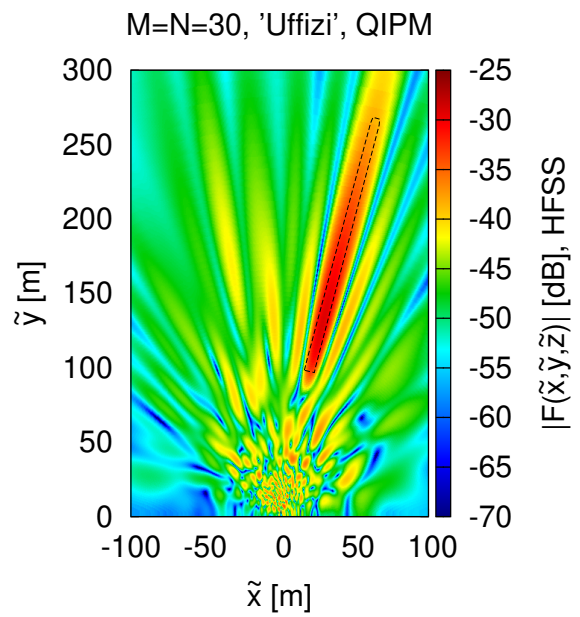
(a)



(b)

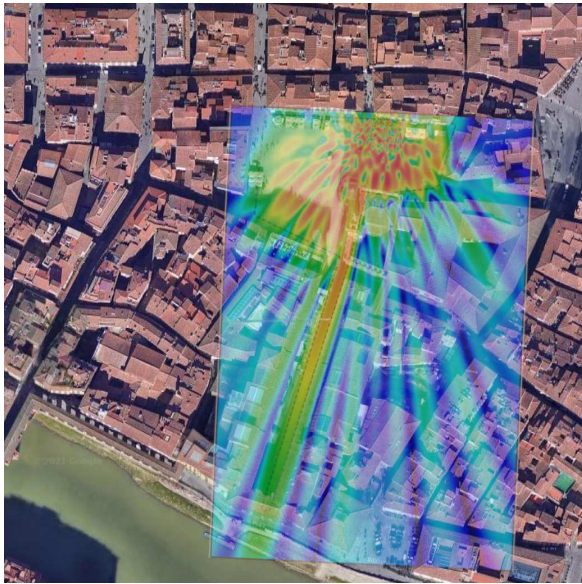


(c)

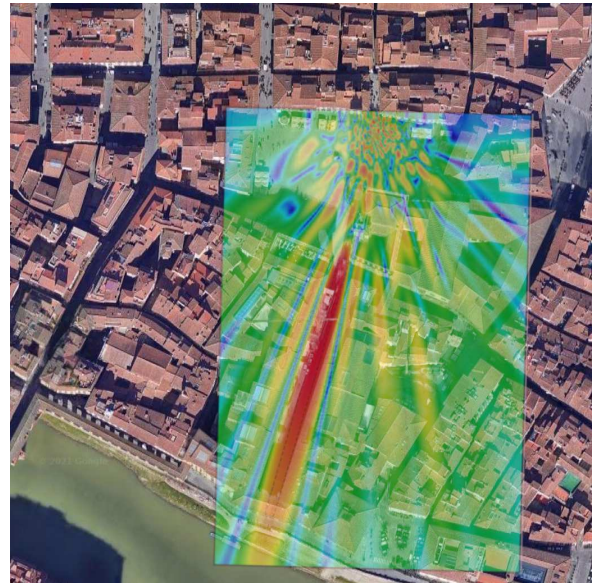


(d)

**Fig. 13** - G. Oliveri et al., “Multi-Scale Single-Bit *RP-EMS* Synthesis for ...”



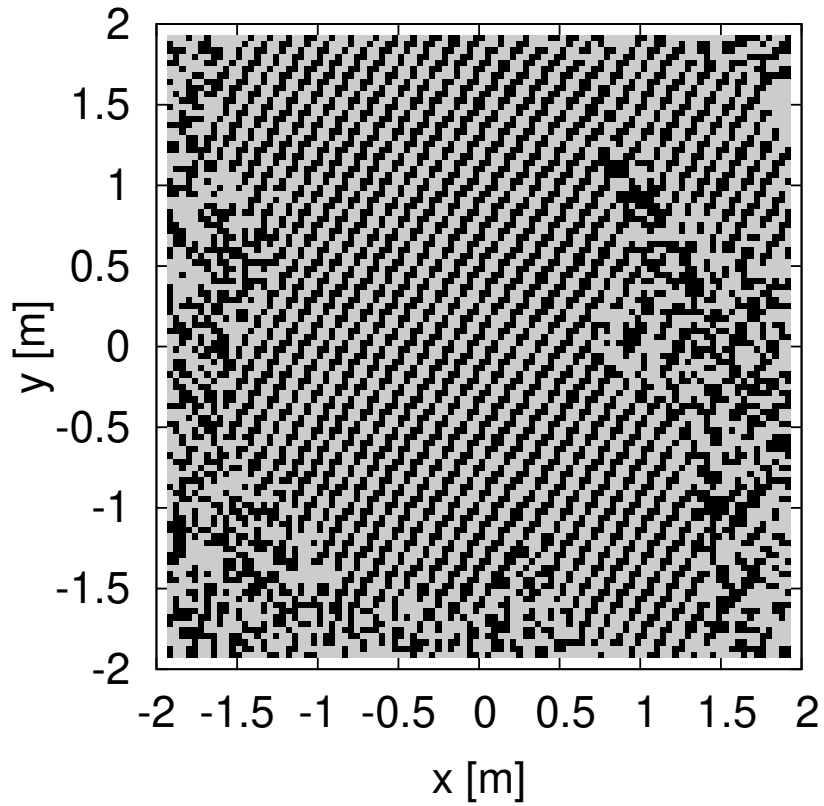
(a)



(b)

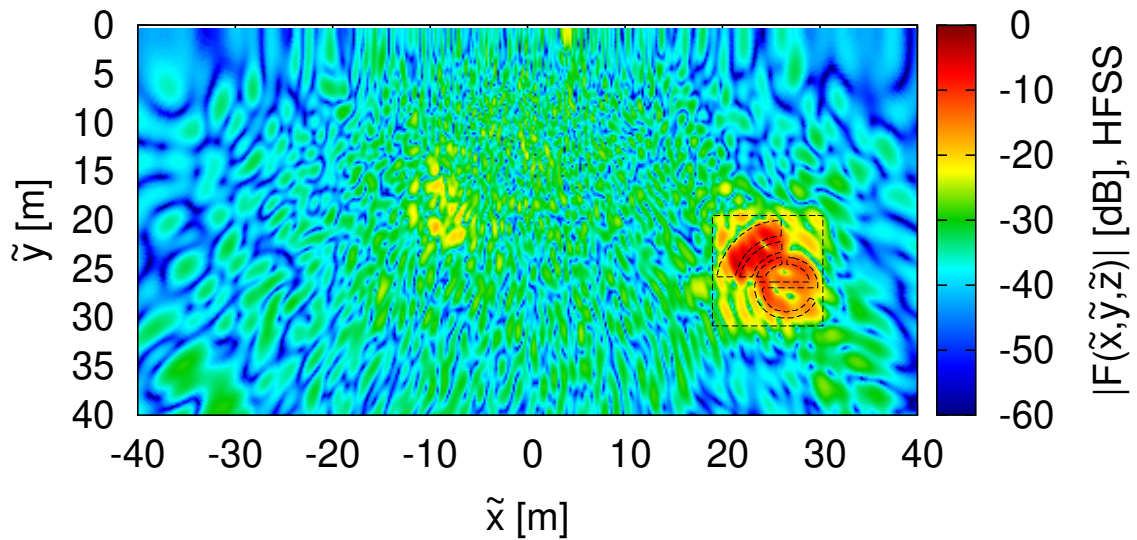
**Fig. 14 - G. Oliveri et al., “Multi-Scale Single-Bit *RP-EMS* Synthesis for ...”**

M=N=100, Footprint 'ELEDIA', QIPM



(a)

M=N=100,  $\tilde{z}=0$  [m], Footprint 'ELEDIA', QIPM



(b)

Fig. 15 - G. Oliveri et al., "Multi-Scale Single-Bit *RP-EMS* Synthesis for ..."

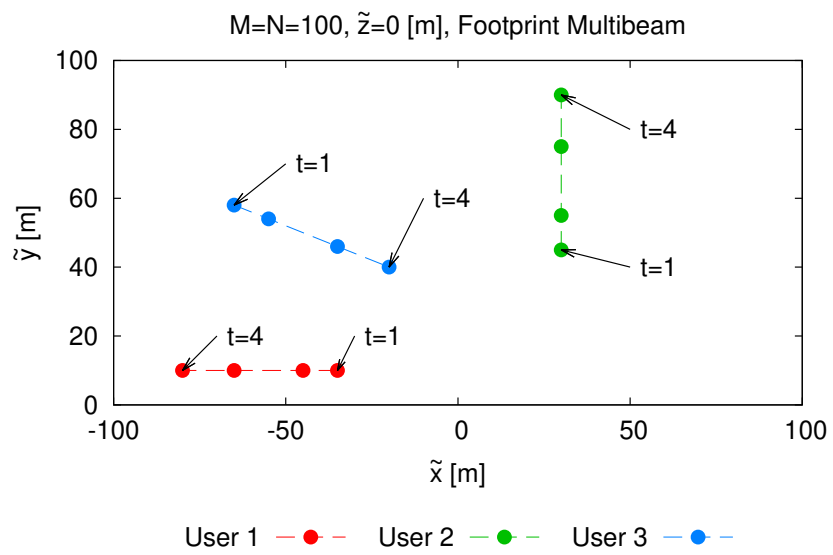


**Fig. 16 - G. Oliveri et al., “Multi-Scale Single-Bit *RP-EMS* Synthesis for ...”**

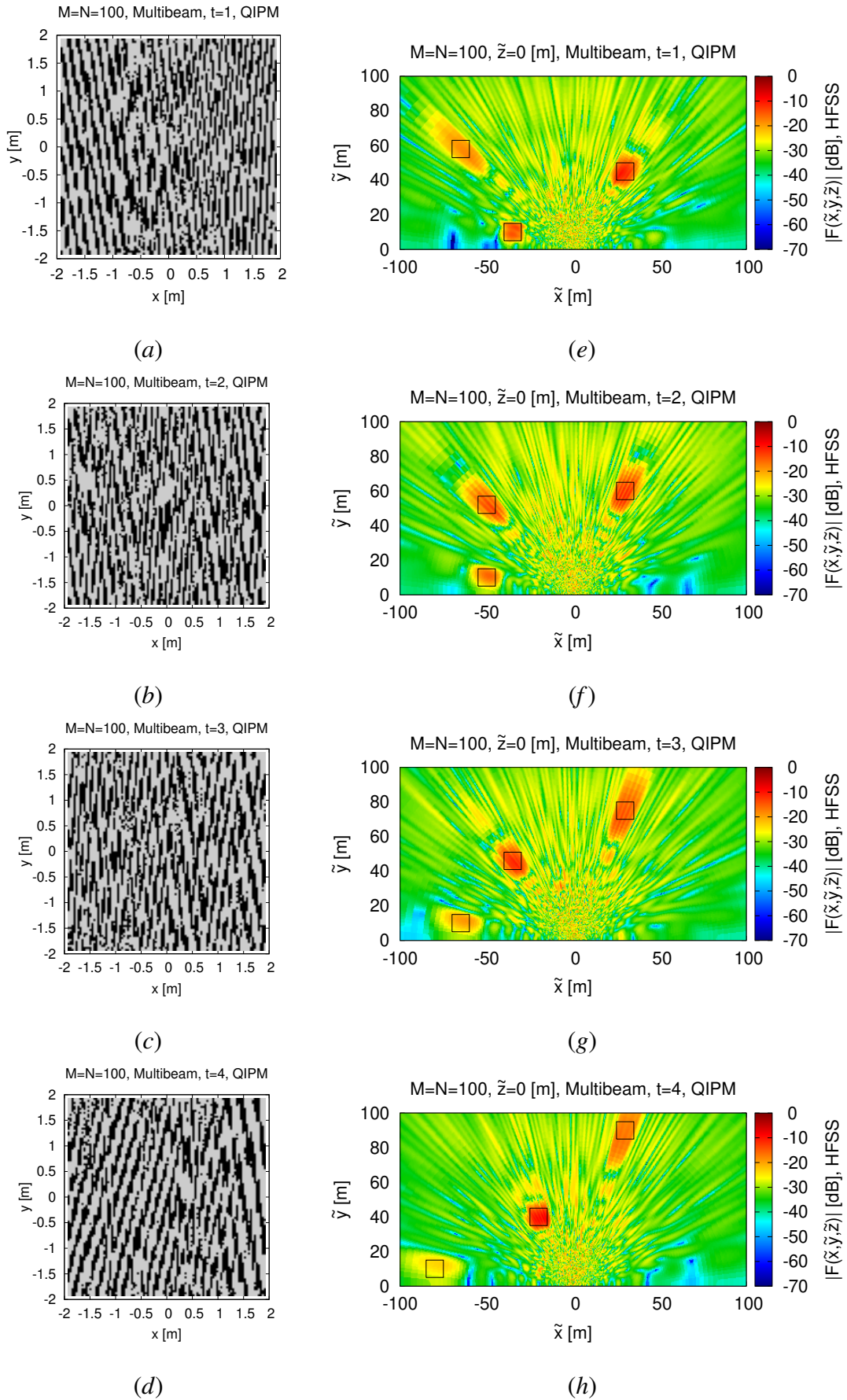


Fig. 17 - G. Oliveri et al., "Multi-Scale Single-Bit  $RP$ -EMS Synthesis for ..."

<i>Parameter</i>	<i>Value [m]</i>
$g_1^{opt} = g_2^{opt}$	$3.854 \times 10^{-2}$
$g_3^{opt} = g_4^{opt}$	$2.191 \times 10^{-2}$
$g_5^{opt} = g_{11}^{opt}$	$1.616 \times 10^{-4}$
$g_6^{opt} = g_{12}^{opt}$	$2.488 \times 10^{-3}$
$g_7^{opt} = g_{13}^{opt}$	$3.300 \times 10^{-4}$
$g_8^{opt} = g_{14}^{opt}$	$1.777 \times 10^{-3}$
$g_9^{opt} = g_{15}^{opt}$	$2.000 \times 10^{-4}$
$g_{10}^{opt} = g_{16}^{opt}$	$6.000 \times 10^{-4}$

**Table I - G. Oliveri et al., “Multi-Scale Single-Bit *RP-EMS* Synthesis for ...”**